Chapter 1

Influence of Solute Atoms on Deformation Behaviour of Selected Magnesium Alloys

Zuzanka Trojanová, Peter Palček, Pavel Lukáč and Zdeněk Drozd

Additional information is available at the end of the chapter

http://dx.doi.org/10.5772/58949

1. Introduction

Magnesium alloys due to their relative high specific strength and low density are used for a wide range of applications – for example in the automobile and transportation industries; they promise significant weight saving. Numerous studies have been performed in order to estimate their mechanical and physical properties. It is well known that many physical and mechanical properties of metals are influenced by alloying. The solute atoms cause an increase in the strengthening of materials. On the other hand, it is difficult to predict the effect of solute atoms on the strength and deformation behaviour of magnesium and its alloys because the experimental data concerning the critical resolved shear stress (CRSS) of single crystals of binary alloys are restricted.

In this chapter we deal with the effect of solute (foreign) atoms on the mechanical properties of magnesium. The foreign atoms are assumed to substitute for the matrix atoms and/or form precipitates. We restrict ourselves mainly to the yield stress and the true stress-true strain curves measured at a constant strain rate at room and higher temperatures. The deformation behaviour of polycrystals is influenced by the presence of crystal defects. Strength of a material is a result of strengthening mechanisms. One of the strengthening mechanisms is solution hardening defined as the increase of the initial flow stress as foreign atoms are dissolved in it [1, 2]. In this chapter original results of authors were used.

2. Fundamentals of plastic deformation

Plastic deformation of magnesium polycrystals occurs by glide of dislocations and/or twinning. Glide of dislocations with the Burgers vector of $1/3[11\bar{2}0]$ on (0001) basal plane is the

easiest slip mechanism; often called basal slip of <***a***> type dislocation. The CRSS is required to activate the glide of <***a***> type dislocations. In order to estimate the CRSS (the stress acting on the slip plane in the slip direction) for a binary magnesium alloy (Mg-X), experimental tests on single crystals are needed. The yield strength of polycrystals is connected with the CRSS of single crystals with help of the relationship $\sigma_y=M\tau_0$, where M is the Taylor orientation factor. The deformation behavior of magnesium and magnesium alloy polycrystals may be influenced by twinning and the activity of non-basal slip systems. Glide of <***a***> dislocations in prismatic planes and glide of<***c+a***> dislocations in the second-order pyramidal slip systems should be consider. However for explanation, it is important to consider not only the solute influence but also the effect of grain size. These factors may affect not only basal slip but also prismatic slip and twinning responsible for the mechanical properties. Crystallographic textures can also change the value of the yield strength as for instance for the case of rolled sheets deformed in the rolling direction [3, 4].

It is widely accepted that the stress necessary for the dislocation motion in the slip plane can be divided into two components:

$$\sigma_D = \sigma_i + \sigma^*, \tag{1}$$

where σ_i is the internal (athermal) contribution to the stress, resulting from long-range internal stresses impeding the plastic flow.

$$\sigma_i = \alpha_1 Gb \rho_t^{1/2}, \tag{2}$$

where G is the shear modulus, σ_1 is a constant describing interaction between dislocations, b is the Burgers vector of dislocations and ϱ_t is the total dislocation density. The effective stress σ^* acts on dislocations during their thermally activated motion when they overcome short range obstacles. The mean velocity of dislocations υ is connected with the plastic strain rate by the Orowan equation:

$$\dot{\varepsilon} = (1/M)\rho_m b v \tag{3}$$

where ϱ_m is the mobile dislocation density. The most common equation used in describing the average dislocation velocity as a function of the effective stress is an Arrhenius type. The plastic strain rate $\dot{\varepsilon}$ for a single thermally activated process can be expressed as:

$$\dot{\varepsilon} = \dot{\varepsilon}_0 \exp\left[-\Delta G\left(\sigma^*\right)/kT\right], \tag{4}$$

where $\dot{\varepsilon}_0$ is a pre-exponential factor containing the mobile dislocation density, the average area covered by the dislocations in every activation act, the dislocation Burgers vector, the vibration frequency of the dislocation line, and the geometric factor. T is the absolute temperature and k is the Boltzmann constant. $\Delta G(\sigma^*)$ is the change in the Gibbs free energy depending on the effective stress (thermal stress)$\sigma^*=\sigma_{ap}-\sigma_i$ and the simple form is

$$\Delta G(\sigma^*) = \Delta G_0 - V\sigma^* = \Delta G_0 - V(\sigma - \sigma_i). \quad (5)$$

Here ΔG_0 is the Gibbs free energy necessary for overcoming a short range obstacle without the stress (the barrier activation energy at zero stress) and V=bdL is the activation volume where d is the obstacle wide and L is the mean length of dislocation segments between obstacles. It should be mentioned that L may depend on the stress acting on dislocation segments. In a stress relaxation (SR) test, the specimen is deformed to a certain stress σ_0 and then the machine is stopped and the stress is allowed to relax. The stress decreases with the time t. The specimen can be again reloaded to a higher stress (load) and the SR test may be repeated. The time derivative $\dot{\sigma}=d\sigma/dt$ is the stress relaxation rate and $\sigma=\sigma(t)$ is the flow stress at time t during the SR. SR tests are very often analysed under the assumption that the SR rate is proportional to the strain rate $\dot{\varepsilon}$ and then $\sigma(t)$ can be expressed according to [5] as:

$$\Delta\sigma(t) = \sigma(0) - \sigma(t) = \alpha \ln(\beta t + 1), \quad (6)$$

where $\sigma(0) \equiv \sigma_0$ is the stress at the beginning of the stress relaxation at time t=0, β is a constant and $\alpha=kT/V$.

3. Mg-Li-Al (LAxy) alloys

3.1. Microstructure of Mg-Li alloys

Among Mg alloys, magnesium-lithium alloys, as the lightest metallic materials, are attractive for a large amount of applications. They are of great importance also for medicine purposes. Therefore, it is important to investigate mechanical properties at different temperatures and to estimate the deformation mechanisms responsible for the deformation behaviour of Mg-Li alloys at elevated temperatures. Pure Mg has hexagonal close packed structure. The density of Mg-Li alloy decreases with an increase of lithium content. The addition of Li increases ductility. The Mg–Li phase diagram shows that Li is soluble in hcp α-phase up to 4 wt%, while Mg alloyed with greater than 12 wt% Li has a bcc structure (β-phase) [6]. Ductility of the hcp α-phase are worse in comparison with the bcc alloys that are very good machinable and weldable. Disadvantages of Mg-Li alloys with bcc structure are a high chemical activity and poor corrosion resistivity. Some compromise would be an alloy with 8 wt% of Li (a mixture of phases $\alpha+\beta$) that might exhibit both improved mechanical properties as well as a good corrosion resistance. In light micrograph in Fig. 1, light α-phase and darker β-phase may be

visible. The alloys were produced by pressure infiltration under an argon pressure (up to 6 MPa) at temperatures of 615-635 K.

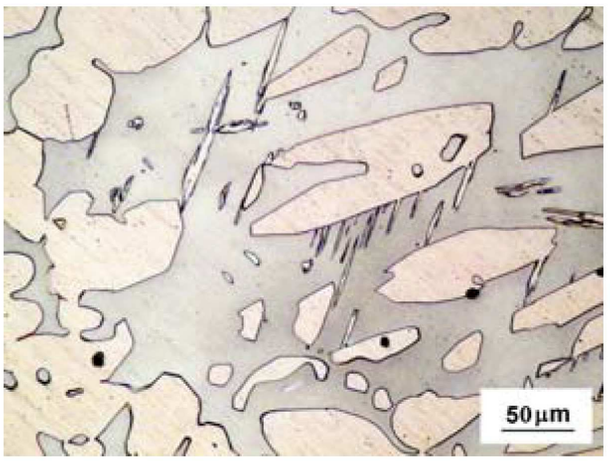

Figure 1. Light micrograph of the Mg8Li alloy.

3.2. Deformation of Mg-Li alloys

Compression tests were performed in an Instron type machine at a constant crosshead speed giving an initial strain rate of 2.4×10^{-4} s^{-1}. The argon atmosphere was used as a protecting atmosphere in the furnace at elevated temperatures. The compression yield stress (CYS), σ_{02}, was estimated as the flow stress at 0.2% offset strain. The ultimate compression strength (MCS), σ_{max}, corresponds to the maximum value of the flow stress. Samples were deformed to a predetermined strain of 0.3, and then deformation was interrupted.

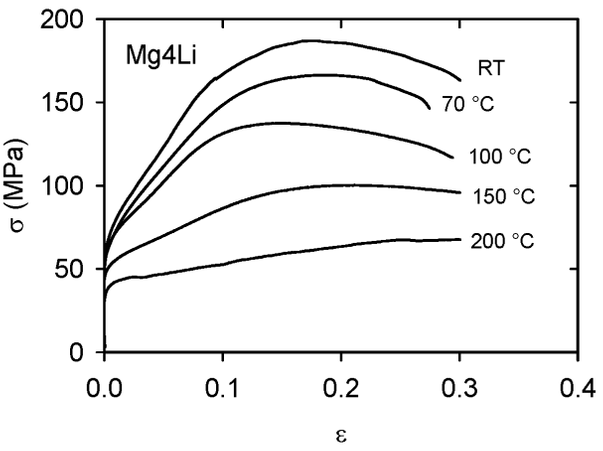

Figure 2. True stress-true strain curves estimated for Mg4Li alloy at various temperatures.

http://dx.doi.org/10.5772/58949

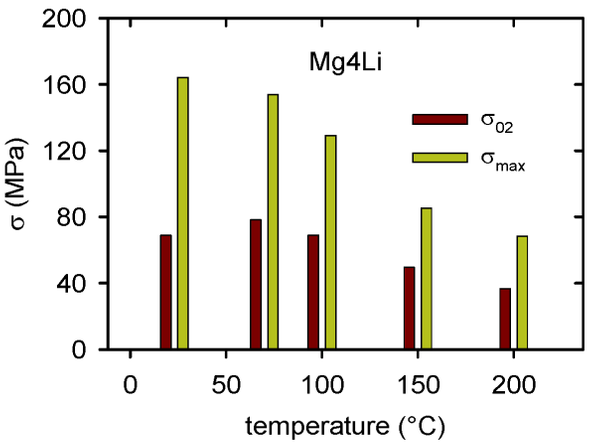

Figure 3. Temperature variation of the CYS and MCS estimated for Mg4Li alloy.

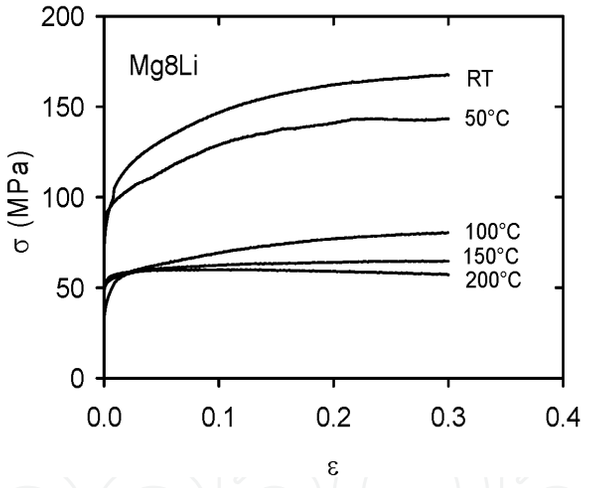

Figure 4. True stress-true strain curves estimated for Mg8Li alloy at various temperatures.

Figure 2 shows the true stress-true strain curves estimated at various temperatures. A significant hardening is obvious especially for lower temperatures. Figure 3 shows the temperature variation of the CYS, σ_{02}, as well as the MCS (σ_{max}) of Mg4Li alloy. It is apparent from Fig. 3 that the temperature variation of CYS exhibits a local maximum at a temperature of 70 °C. The MCS of Mg-4Li alloy decreases rapidly with increasing temperature. The differences between MCS and CYS exhibit a rapid decrease with increasing temperature. The true stress-true strain curves of Mg-8Li alloy measured in compression at various temperatures are shown in Fig. 4. A rapid decrease of the flow stresses at temperatures higher than 50 °C is obvious in Fig. 5. The temperature variation of the CYS exhibits a local maximum at 50 °C.

While the stress-strain curves estimated for Mg4Li exhibit a significant strain hardening, the curves observed for Mg12Li are very flat (Fig. 6); the difference between the CYS and MCS is relatively low and decreases with increasing temperature (Fig. 7).

The Mg-4Li alloy has *hcp* structure. The addition of Li to Mg increases the critical resolved shear stress (CRSS) for basal slip; the solid solution hardening is observed [7]. The CRSS of Mg4Li is almost independent on the temperature above room temperature while the CRSS for non-basal slip decreases with temperature below 200 °C as shown in [8]. The addition of Li causes a decrease of both ***a*** and ***c*** lattice parameters in Mg-Li solid solution [9].

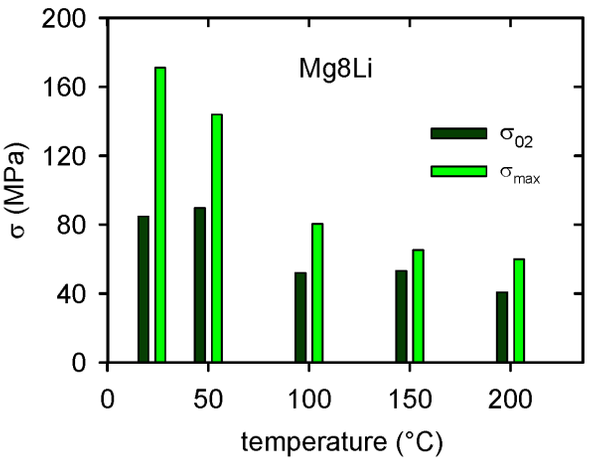

Figure 5. Temperature variation of the CYS and MCS estimated for Mg8Li alloy.

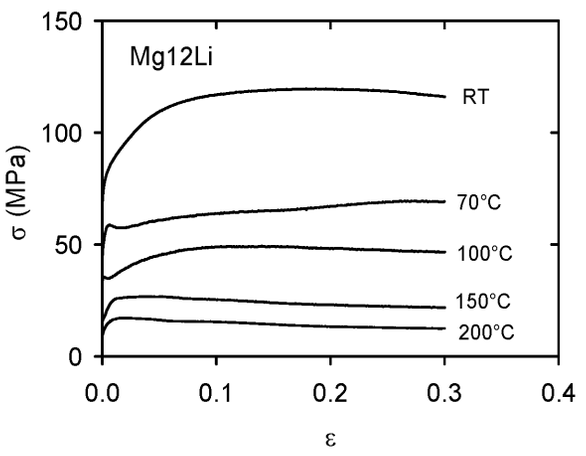

Figure 6. True stress-true strain curves of Mg12Li alloy at various temperatures.

http://dx.doi.org/10.5772/58949

It is well known that the dominant slip system in Mg and *hcp* Mg alloys at room temperature is the basal one. To fulfil von Mises criterion, a non-basal slip system should be active. The activity of non-basal slip systems plays an important role in dynamic recovery (softening). The pyramidal slip systems can be considered as non-basal slip systems. During deformation of magnesium alloy polycrystals, the motion not only **<a>** (basal) dislocations but also ***<c+a>*** (pyramidal) dislocations is assumed. Screw components of the <*c*+*a*> dislocations can move to the parallel slip planes by double cross slip and then annihilate, which causes a decrease in the strain hardening rate; softening is observed. With the addition of Li the c/a ratio decreases, which may result in a higher activity of non-basal slip [10]. Agnew et al. [11] revealed that the <*c*+*a*> dislocations in the pyramidal planes improve ductility of MgLi alloys. Pawelek et al. [12] studying acoustic emission from deformed Mg-Li alloys estimated a high level of acoustic emission in Mg4Li alloy as a result of non-basal slip in the prismatic and pyramidal slip systems.

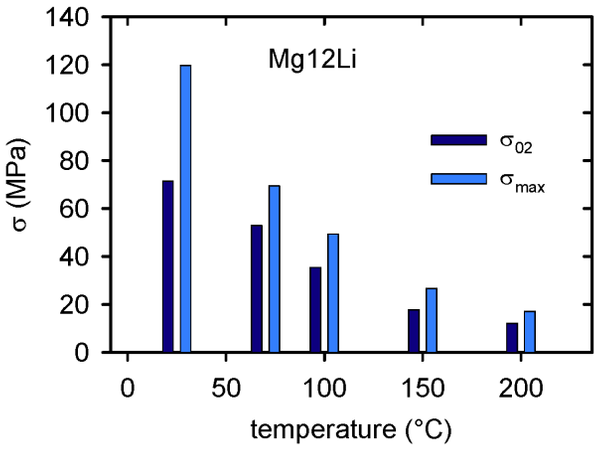

Figure 7. Temperature variation of the CYS and MCS estimated for Mg12Li alloy.

3.3. Microstructure of Mg-xLi-yAl alloys

To improve the mechanical properties, alloying with other elements can be used. The addition of Al atoms to Mg4Li causes the formation of precipitates. A combination of two different hardening mechanisms should be considered: solid solution hardening and precipitation hardening. The microstructure of as-cast Mg8LixAl alloys under consideration consists essentially of *hcp* magnesium-based α-phase and *bcc* lithium-based one (β-phase) and AlLi precipitates as well. Accordingly, interpenetrated (α+β) matrix structure with dominating α-phase is characteristic for LA83 and LA85 (see Fig. 8) alloys. Light micrograph of the Mg12Li3Al (LA123) alloy shows that the alloy does not contain only one phase (Fig. 9). Both phases (α and β) are present contrary to the alloy without Al because aluminium stabilises the *hcp*α-phase.

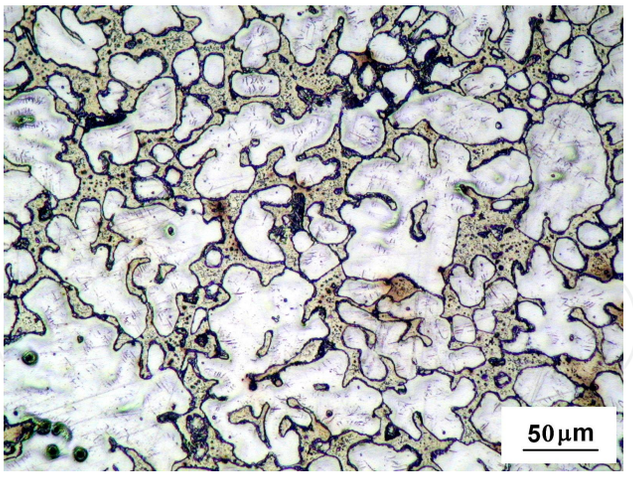

Figure 8. Light micrograph of the Mg8Li5Al alloy.

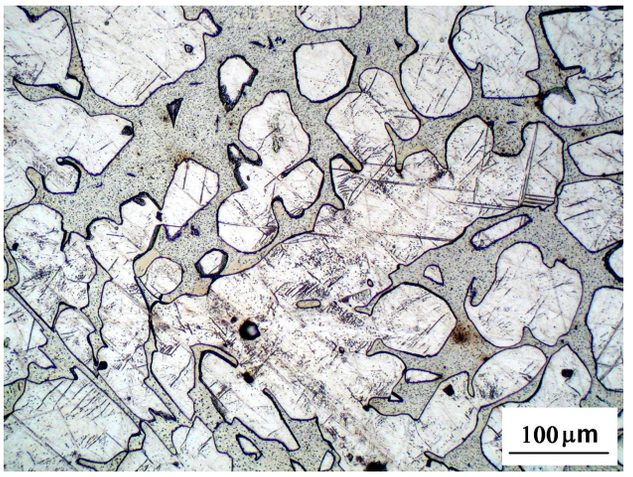

Figure 9. Light micrograph of the Mg12Li3Al.

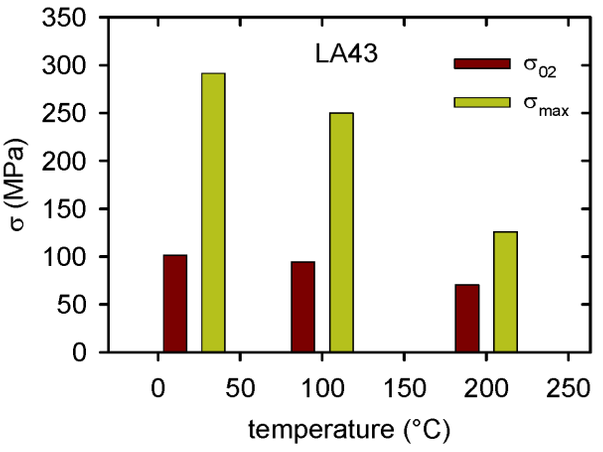

Figure 10. Temperature variation of the CYS and MCS estimated for Mg4Li3Al alloy.

http://dx.doi.org/10.5772/58949

3.4. Deformation of Mg-xLi-yAl alloys

The temperature dependence of the CYS and MCS estimated for LA43 (Mg-4Li-3Al) and LA45 (Mg-4Li-5Al) are introduced in Figs. 10 and 11. High differences between CYS and MCS, especially observed at lower temperatures, and moderate decrease of the characteristic stresses with temperature indicate significant hardening during plastic deformation. The presence of AlLi precipitates influences not only the yield stress but also the storage of dislocations during plastic deformation. In the LA43 (Mg4Li3Al) and LA45 (Mg4Li5Al) alloys, there are obstacles of non-dislocation types such as precipitates and the dislocation obstacles (forest dislocations). The observed high difference between the CYS and MCS indicates a significant hardening during the deformation process. A part of the moving dislocations stored at the obstacles contributes to hardening. On the other hand, processes such as cross slip and climb of dislocations contribute to softening– the difference between CYS and MCS decreases with increasing deformation temperature. The dislocation microstructure can change. For simplicity, the total dislocation density is considered as the characteristic parameter of the evolution of microstructure during deformation. According to the model of Lukáč and Balík [13], we take into account storage of dislocations at both impenetrable obstacles and forest dislocations, and annihilation of dislocations due to both cross slip and climb.

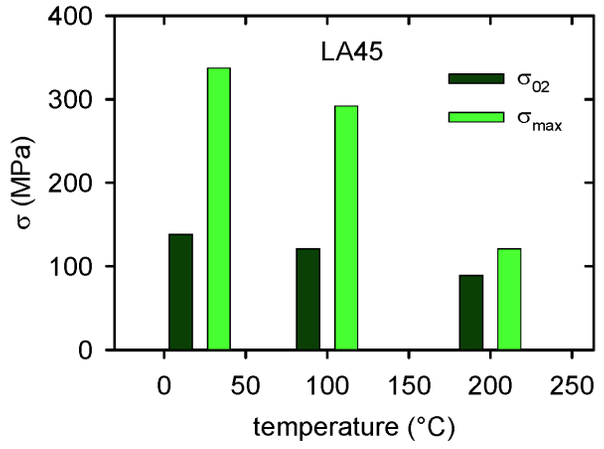

Figure 11. Temperature variation of the CYS and MCS estimated for Mg4Li5Al alloy.

The true stress-true strain curves of LA85 alloy estimated at various temperatures are shown in Fig. 12. The strain hardening is observed at temperatures up to 100 °C; the stress-strain curves obtained at higher temperatures are flat. The temperature variations of the CYS and MCS for LA83 and LA85 alloys are shown in Figs. 13 and 14. The strengthening effect of Al atoms in the case of LA85 alloy has been found to be really high even at 100 °C. A moderate decrease of both characteristic stresses with temperature classes this alloy as a material for industrial applications.

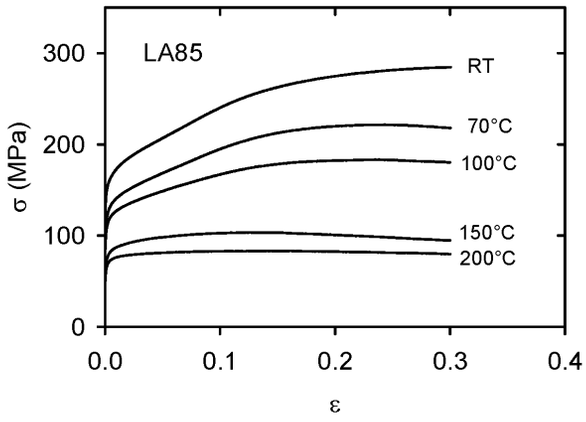

Figure 12. True stress-true strain curves of Mg8Li5Al alloy at various temperatures.

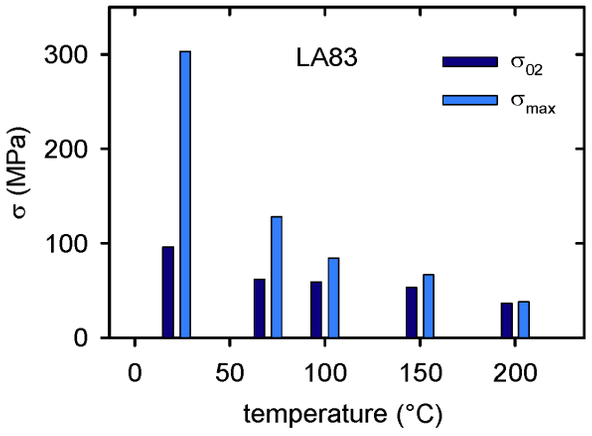

Figure 13. Temperature variation of the CYS and MCS estimated for Mg8Li3Al alloy.

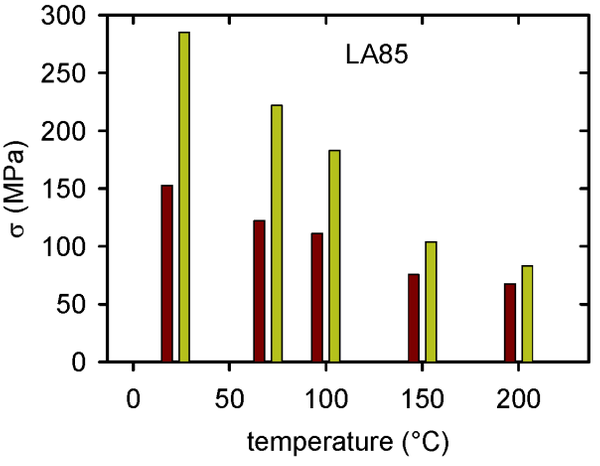

Figure 14. Temperature variation of the CYS and MCS for Mg8Li5Al alloy.

http://dx.doi.org/10.5772/58949

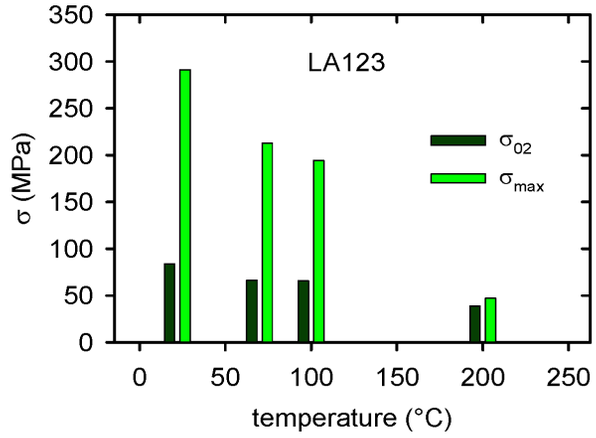

Figure 15. Temperature variation of the CYS and MCS estimated for Mg12Li3Al.

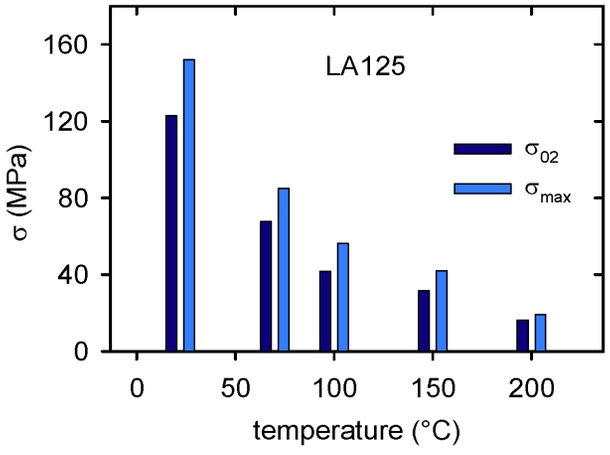

Figure 16. Temperature variation of the CYS and MCS estimated for Mg12Li5Al.

The temperature variations of both CYS and MCS are shown for LA123 and LA125 alloys in Figs. 15 and 16, respectively. The CYS is significantly higher for the alloy containing 5% of Al, while MCS exhibits higher values for the LA123 alloy. Thermal stability is higher in the case of LA125 alloy. The influence of Al on the mechanical characteristics of Mg-Li alloys at two temperatures is summarised in Table 1.

	LA40	LA43	LA45	LA80	LA83	LA85	LA120	LA123	LA125
					RT				
CYS (MPa)	68.9	103.7	138.4	84.8	96.2	152.7	71.4	83.9	122.8
MCS (MPa)	164.3	237.0	337.4	171.2	302.9	285.0	119.6	291.2	152.1
					100 °C				
CYS (MPa)	60.0	121.8	121.2	52.1	62.0	111.4	35.5	65.9	41.7
MCS (MPa)	129.0	292.0	292.0	80.5	84.3	183.0	49.4	194.5	84.8

Table 1. Influence of Al addition on CYS and MCS of Mg4Li, Mg8Li and Mg12Li alloys.

To conclude it is possible to say that the best mechanical properties of the superlight MgLi alloys were found for Mg8Li alloy with 5 wt% of Al. Combining of the stronger α phase with a more ductile β phase results in a material with the high specific strength.

4. Mg-Al-Sr (AJxy) alloys

4.1. Microstructure of the Mg-Al-Sr alloys

Special industrial applications require improvement of the high temperature properties. For these elevated temperature applications, alloys containing rare earth elements have been developed. New Mg-Al-Sr alloys are being developed with the aim to find cast alloys with good creep resistance and good strength and replace expensive rare earth alloying elements with some cheaper one. Pekguleryuz [14] reported that Mg-Al-Sr alloys show different microstructures based on the Sr/Al ratio. For Sr/Al ratio below about 0.3, only Al_4Sr intermetallic phase is present as the second phase in the structure. When the Sr/Al ratio is higher, a second intermetallic phase, a new, ternary Mg-Al-Sr compound, is observed. When the Sr/Al ratio is very low, there is insufficient amount of Sr to bind all Al atoms and the excess Al would form the $Mg_{17}Al_{12}$ phase. Figure 17 shows light micrograph of the squeeze cast AJ51 alloy. The primary Mg grains are surrounded by the interconnected network of the grain boundary phase. This phase is formed during solidification process and it has lamellar type morphology. The γ phase ($Mg_{17}Al_{12}$) is accompanied with Al_4Sr phase. Single items are better visible in Figs. 18 and 19, where SEM of AJ91 alloy is presented. Eutectic γ phase forms either continuous shapes or discontinuous precipitates. Light needles visible in both pictures are the Al_4Sr precipitates. Line scan of alloying elements present in particles shown in Fig. 19 is given in Fig. 20. Line scan analysis was performed along the light arrow showed in Fig. 19. Small content of Sr is present in the δ solid solution; higher in the position of a needle shaped particle.

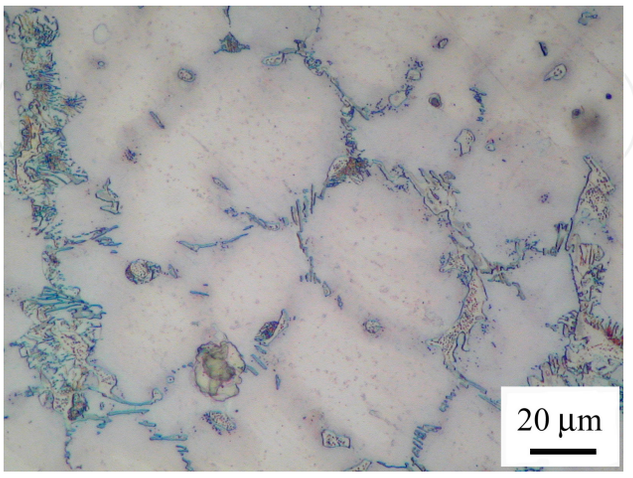

Figure 17. Light micrograph of the AJ51 alloy.

http://dx.doi.org/10.5772/58949

4.2. Deformation of the AJ alloys

The true stress-true strain curves of AJ51 alloy deformed in compression at various temperatures are shown in Fig. 21. Samples were deformed either to failure or the tests performed at temperatures higher than 100 °C were interrupted at a predetermined strain. Significant hardening at temperatures up to 150 °C is obvious. The curves obtained at temperatures higher are more or less flat – hardening and softening processes are in equilibrium.

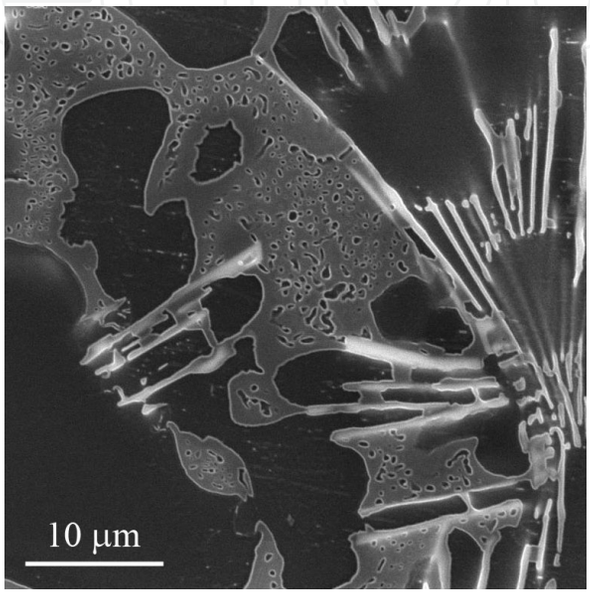

Figure 18. Scanning electron micrograph of as cast AJ91 alloy.

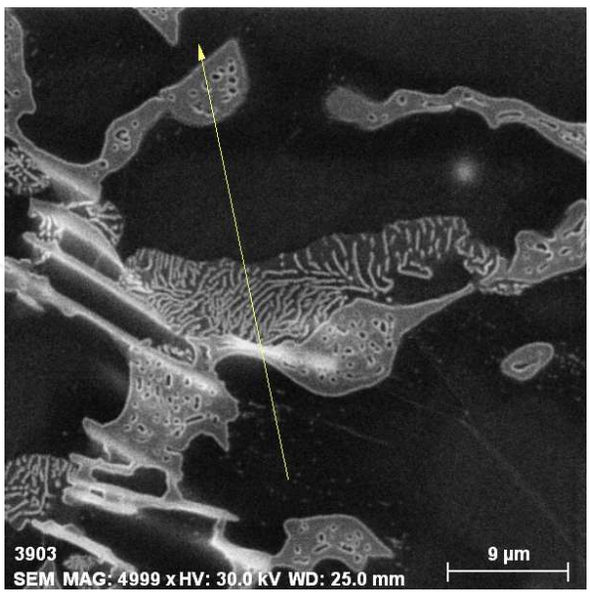

Figure 19. Scanning electron micrograph of as cast AJ91 alloy (different place).

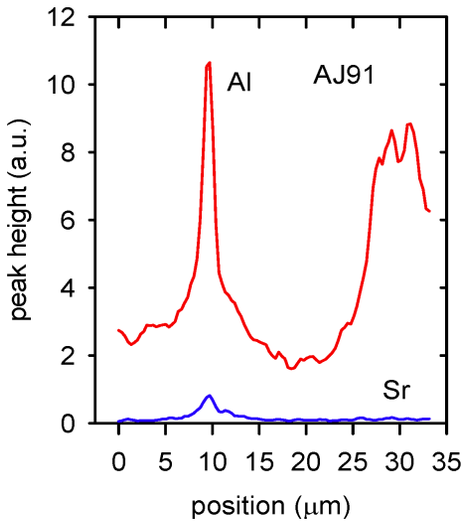

Figure 20. Line scan of alloying elements.

Figure 22 shows the temperature variation of the CYS as well as the MCS. Similar characteristics estimated in tension are shown in Fig. 23. While the values of the yield stress are practically the same for tension and compression, the values of the maximum stress are higher in compression tests. It is a consequence of higher ductility of the alloy in compression and significant hardening during plastic deformation at lower temperatures. The yield stress decreases with increasing temperature for samples deformed in compression. A small local maximum in the temperature dependence of the yield strength observed in the vicinity of 50 °C was observed in several Mg alloys and composites [15]. It is likely caused by a dynamic age hardening.

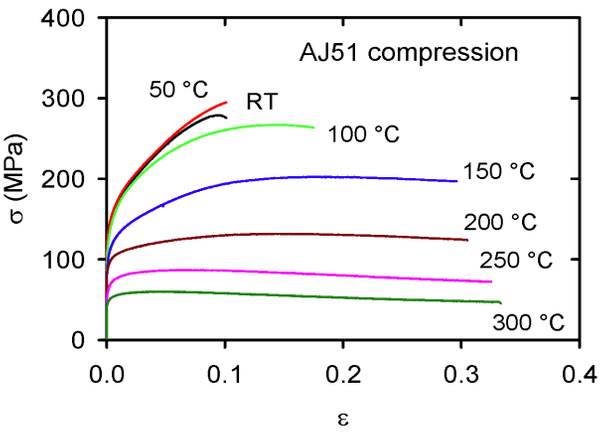

Figure 21. True stress-true strain curves estimated in compression for AJ51 alloy at various temperatures.

The true stress-true strain curves estimated for AJ91 alloy in compression are presented in Fig. 24. The values of the CYS and TYS (Figs. 25 and 26) are higher than the yield stress of the mostly used cast alloy AZ91. The temperature variations of MCS and MTS are shown in Figs. 25 and

http://dx.doi.org/10.5772/58949

26. Ductility of AJ91 alloy deformed in tension is low, at ambient temperature only several percent. Thermal stability is in comparison with AZ91 alloy also better; the CYS as well as TYS do not decrease with increasing test temperature up to 200 °C below 100 MPa. It is done by the thermal stability of Al_4Sr precipitates. Solid solution hardening plays in this case only minor role.

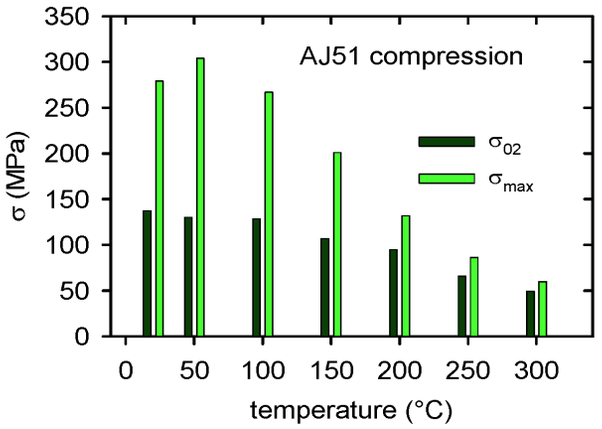

Figure 22. Temperature variation of CYS and MCS for AJ51 alloy.

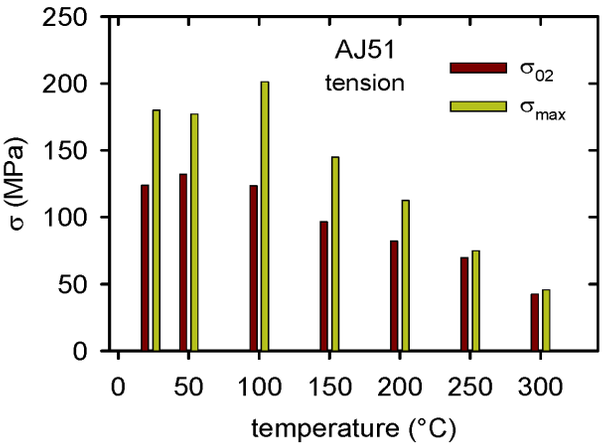

Figure 23. Temperature variation of TYS and MTS for AJ51 alloy.

4.3. Stress components in the AJ alloys

Stress necessary for dislocation motion is possible, according to eq. (1), divided into two components. The components of the applied stress (σ_i, σ^*) may be estimated using Li's method [16]. The SR curves are fitted to the power law function in the form:

$$\sigma - \sigma_i = \left[a\left(m-1\right)\right]^{\frac{1}{1-m}} \left(t + t_0\right)^{\frac{1}{1-m}}, \tag{7}$$

where a, t_0 and m are fitting parameters. The influence of solute atoms on both stress components of AJ51 and AJ91 is obvious from Figs 27-29; it was estimate at three temperatures. At room temperature, an increase in the concentration of solute atoms influences only the internal stress. The observed increase of the internal stress is due to higher density of impenetrable precipitates which are obstacles for the dislocation motion. The effective stress σ* is practically the same for both alloys. From Fig. 27 it is obvious that the internal stress in both alloys is extremely high; it represents more than 90% of the applied stress. The difference between the internal stress of AJ51 and AJ91 alloys at 100 °C (Fig. 28) is relatively high and it indicates the reinforcing effect of the increased concentration of solute atoms. The effective stress is still for both alloys practically the same but the values of σ^* for both alloys are higher in comparison with the values obtained at room temperature. The internal stress estimated for AJ91 alloy at 200 °C (Fig. 29) is for strains up to approximately ε~ 0.08 higher as the effective stress. While the internal stress for AJ91 alloy decreases with strain, the effective stress continuously increases for both alloys. The decrease of the internal stress with strain estimated for both alloys is a consequence of the intensive activity of softening processes. This mechanism will be discussed in details later.

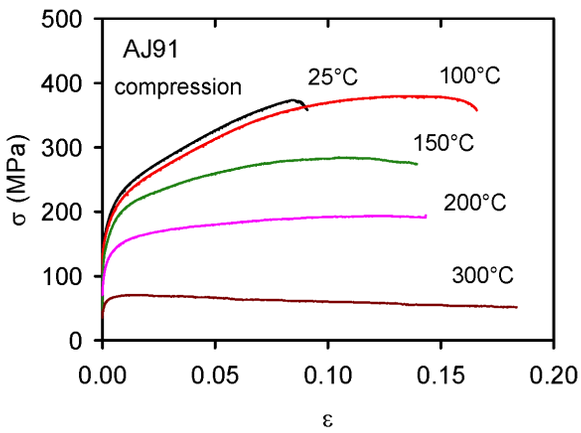

Figure 24. True stress-true strain curves of AJ91alloy deformed in compression at various temperatures.

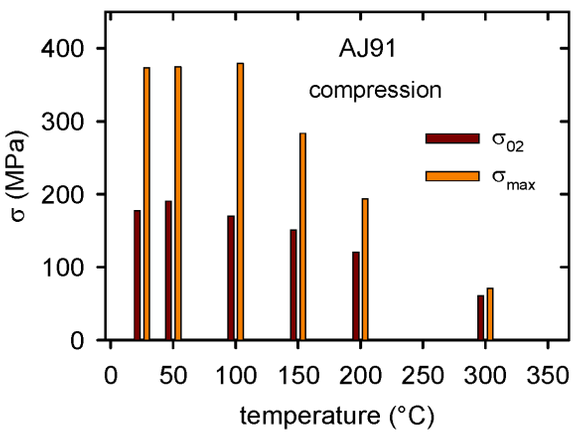

Figure 25. Temperature variation of CYS and MCS for AJ91 alloy.

http://dx.doi.org/10.5772/58949

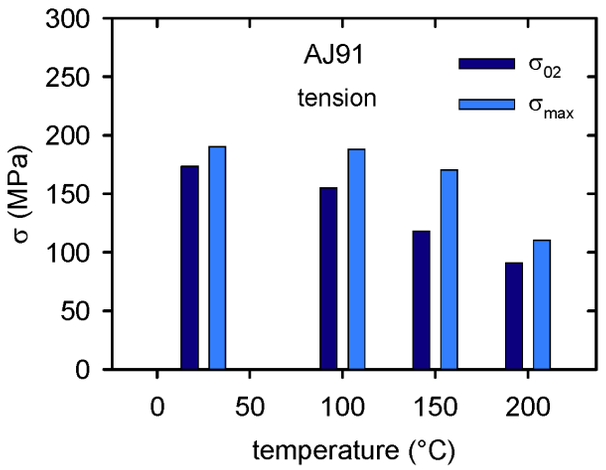

Figure 26. Temperature variation of TYS and MTS for AJ91 alloy.

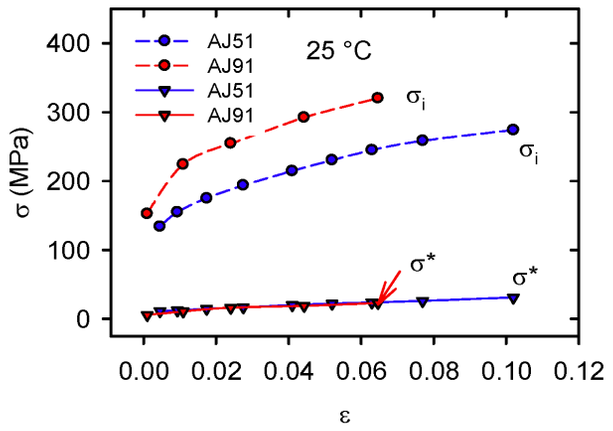

Figure 27. Strain dependence of the internal stress, σ_i, and effective stress, σ^*, for AJ51 and AJ91 alloys deformed at 25 °C

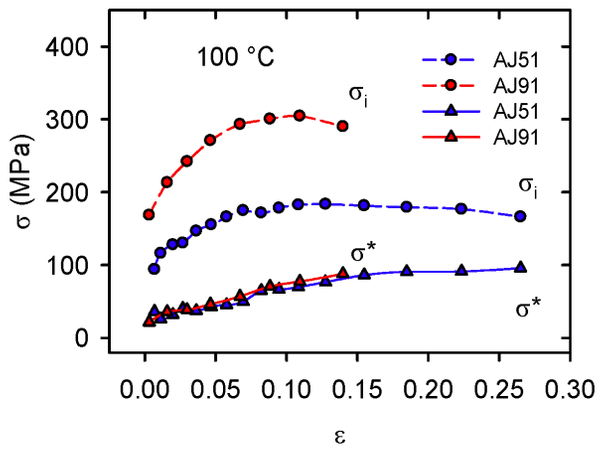

Figure 28. Strain dependence of the internal stress, σ_i, and effective stress, σ^*, for AJ51 and AJ91 alloys at 100 °C.

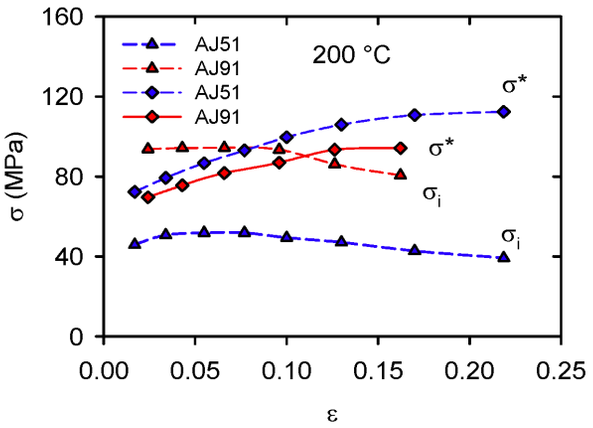

Figure 29. Strain dependence of the internal stress, σ_i, and effective stress, σ^*, for AJ51 and AJ91 alloys at 200 °C.

5. Mg-Al-Ca (AXxy) alloys

5.1. Microstructure of the AX alloys

When Ca is added to Mg-Al binary alloys, the type of precipitating compound depends on the Ca/Al mass ratio. When this ratio is higher than 0.8 the presence of both Mg_2Ca and Al_2Ca were detected. They may contribute to a considerable increase in hardness and the yield stress [17]. For the ratio below 0.8 only Al_2Ca Laves phase (C15-cubic) was observed to have been formed. Both types of precipitates were observed to form along the grain boundaries [18]. Gjestland et al. [19] showed that the creep resistance of AX alloy at 150 °C is similar to magnesium alloys containing rare earths with the added benefit of good corrosion resistance. Terada et al. [20] studied the creep mechanisms in the Mg-5Al-1.7Ca alloy. They found a change of deformation mechanism at the vicinity of 150 °C. Microstructure and mechanical properties of Mg-Al based alloy with Ca addition (AX series) were investigated by Du et al. [21]. They estimated that the small amount of Ca increased the thermal stability of $Mg_{17}Al_{12}$ intermetallic phase, so that the creep resistance at elevated temperatures was improved.

Microstructure of the squeeze cast AX41 alloy used in this study exhibits typical dendritic structure with γ Mg grains decorated by particles. SEM showed the details of the particles structure (Fig. 30); $Mg_{17}Al_{12}$ intermetallic phase surrounded with smaller particles of Al_2Ca. Microstructure of the squeeze cast AX91 alloy is displayed in Fig. 31. Two types of particles were identified, which is better evident in the back scattered electrons image (see Fig. 32). Dark particles in Fig. 32 are eutectics $Mg_{17}Al_{12}$; lighter skeleton-like particles containing Ca atoms.

http://dx.doi.org/10.5772/58949

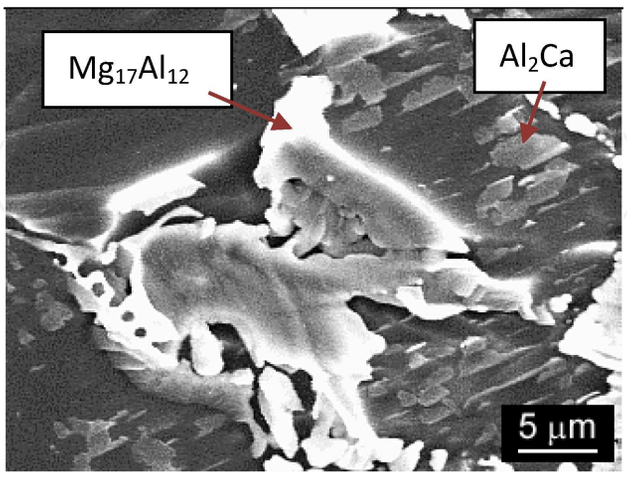

Figure 30. Scanning electron micrograph of as cast AX41 alloy showing the main phases present in the alloy.

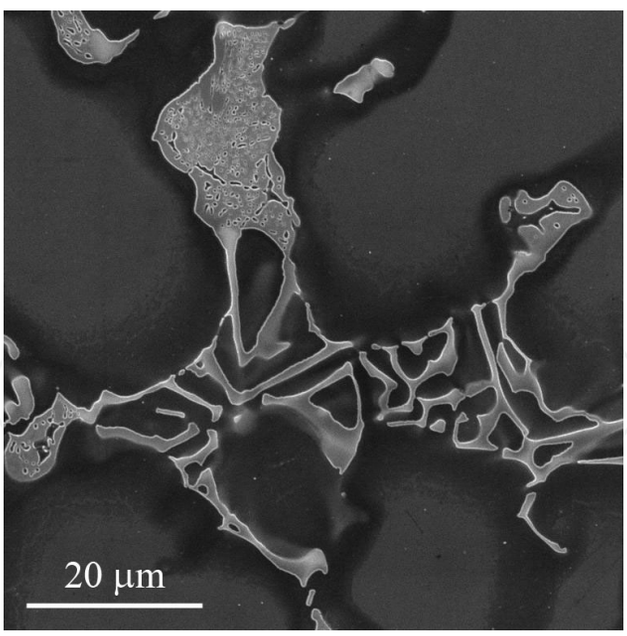

Figure 31. Scanning electron micrograph showing two main phases present in the AX91 alloy. The skeleton-like phase contains Ca.

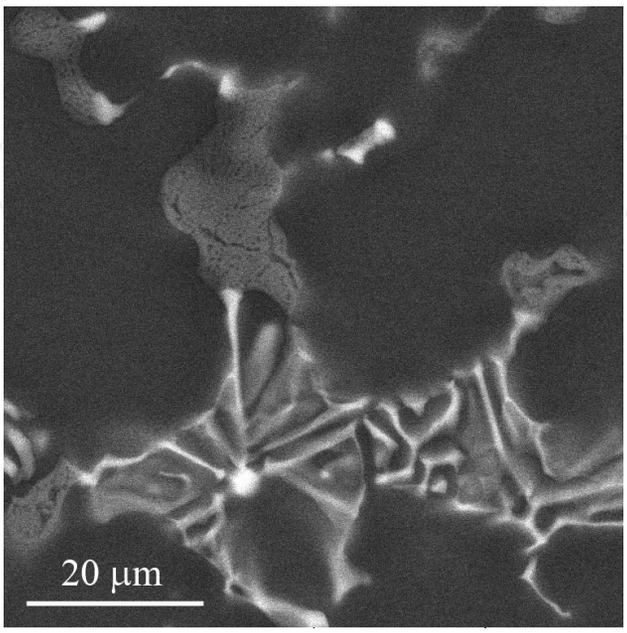

Figure 32. Back scattered electrons image of the same place as showed in Fig. 31.

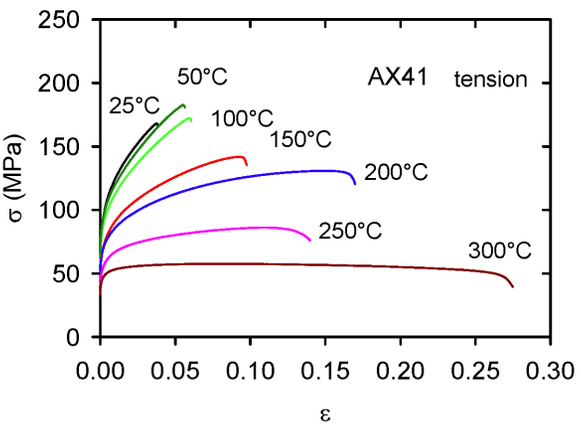

Figure 33. True stress-true strain curves of AX41 alloy deformed in tension at various temperatures.

http://dx.doi.org/10.5772/58949

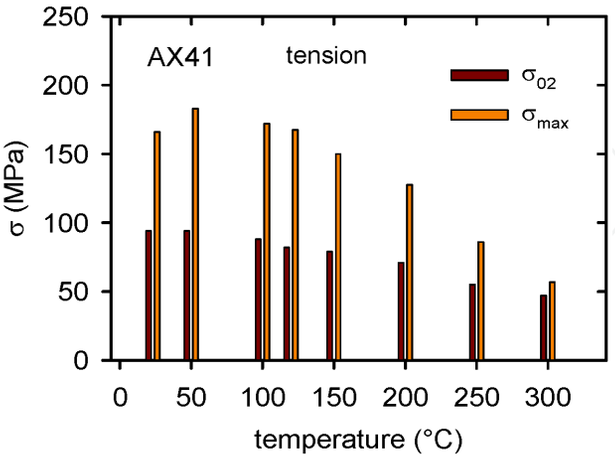

Figure 34. Temperature variation of TYS and MTS for AX41 alloy.

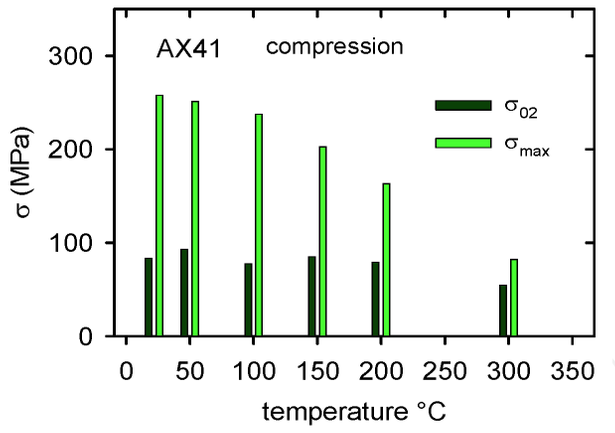

Figure 35. Temperature variation of CYS and MCS for AX41 alloy.

5.2. Deformation of the AX alloys

The true stress-true strain curves of AX41 alloy deformed in tension are presented in Fig. 33. Low ductility (about 5%) of the alloy was observed at lower temperatures below 100 °C; at higher temperatures ductility increases up to 27%. The temperature variations of the TYS and MTS are presented in Fig. 34.

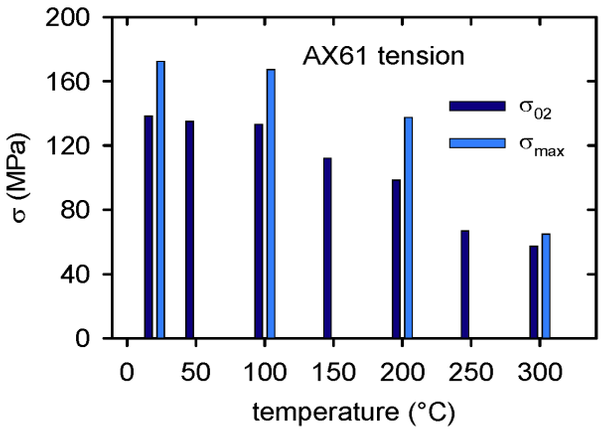

Figure 36. Temperature dependence of TYS and MTS for AX61 alloy.

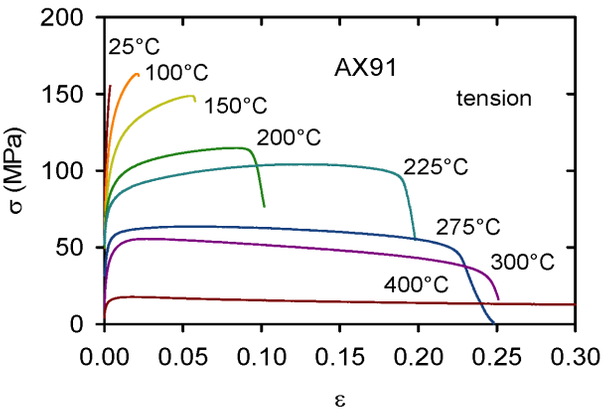

Figure 37. True stress-true strain curves of AX91 alloy deformed in tension at various temperatures.

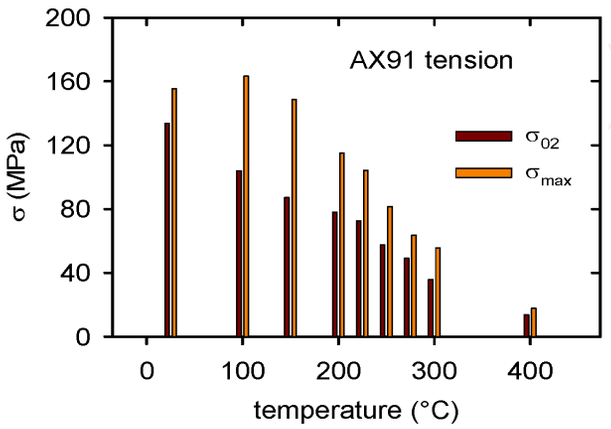

Figure 38. Temperature variation of TYS and MTS for AX91 alloy.

http://dx.doi.org/10.5772/58949

Analogously the values of the CYS and MCS at different temperatures are shown in Fig. 35. It can be seen that the TYS decreases with increasing temperature monotonously whereas the temperature variation of the CYS exhibits a local maximum at about 50 °C. The temperature variations of the TYS and MTS for squeeze cast AX61 alloy are presented in Fig. 36. The values of the TYS are relatively high and decrease only slightly with increasing temperature exhibiting at 200 °C still a value about 100 MPa. The true stress-true strain curves of AX91 alloy measured in tension at various temperatures are shown in Fig. 37. It is obvious from Fig. 37 that ductility of the alloy at temperatures up to 100 °C is limited; it increases up to 25 % at a temperature of 300 °C. The TYS at room temperature was estimated to be approximately equal to that measured for AX61 alloy. The observed rapid decrease of TYS of AX91 with temperature indicates a lower thermal stability of this alloy (Fig. 38). It is a different situation in comparison to the AJ91 alloy, for which the strength was found to be superior.

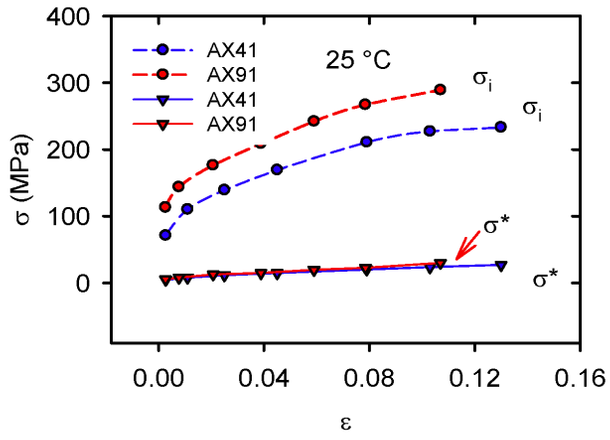

Figure 39. Strain dependence of the internal (σ_i) and effective (σ^*) stresses at 25 °C.

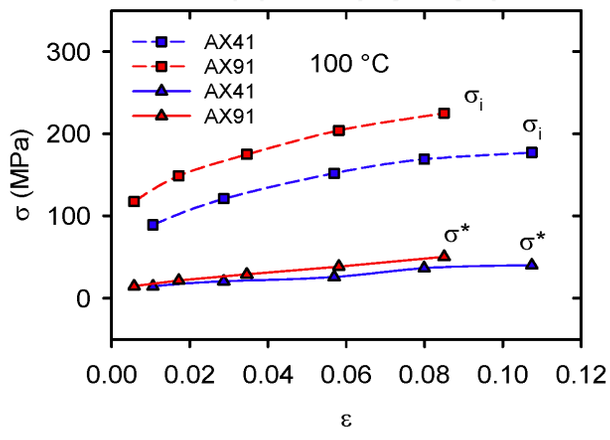

Figure 40. Strain dependence of the internal (σ_i) and effective (σ^*) stresses at 100 °C.

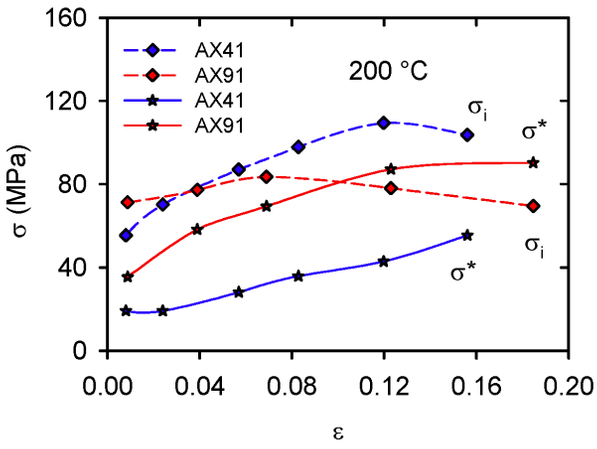

Figure 41. Strain dependence of the internal (σ_i) and effective (σ^*) stresses at 200 °C.

5.3. Stress components in the AX alloys

The applied stress components, σ_i, and, σ^*, for AX41 and AX91 alloys were estimated at three temperatures in compression (see Figs. 39-41). At lower temperatures, 25 and 100 °C, the solute atom concentration influences only the internal stress. The effective stress is for both alloys the same (at 25°C) or it is a bit higher (at 100 °C) for AJ91 alloy. In both cases the effective stress slightly increases with increasing strain. A different behaviour was found at 200 °C. While the internal stress estimated for AX41 alloy increases with increasing strain up to 12%, the internal stress in AX91 alloy slightly increases with strain up to 8% and then decreases. On the other hand, the effective stress increases in the whole strain range.

According to eq. (2) the internal stress, σ_i is proportional to $\varrho^{1/2}$ where ϱ is the density of dislocations. The internal stress, σ_i, generally, reflects the resistance of a metallic material against plastic deformation. Considering a constant microstructure, the deformation (flow) stresses are done by the evolution of the dislocation density with strain and temperature. The observed increase of the internal stress for all alloys AJ and AX series indicates an increase in the dislocation density. The moving dislocations can be stored at both non-dislocation and dislocation type obstacles. Non-dislocation obstacles may be grain boundaries, non-coherent precipitates and/or twins; the dislocation type obstacles are formed by reactions between dislocations. As mentioned in paragraph 2, in *hcp* magnesium alloys dislocations with the Burgers vector **<*a*>**=$1/3[11\bar{2}0]$ may glide in basal, prismatic, and first−order pyramidal planes. Dislocations with the Burgers vector <*c*+*a*>=$1/3[11\bar{2}3]$ can glide in the first− and second−order pyramidal planes. The basal <*a*> dislocations may react with the pyramidal <c+*a*>dislocations according to:

$$\tfrac{1}{3}\langle 2\bar{1}\bar{1}3\rangle + \tfrac{1}{3}\langle \bar{2}110\rangle \rightarrow \langle 0001\rangle. \tag{8}$$

The resulting sessile**<*c*>** dislocations with the Burgers vector parallel to the c axis are not able to glide in the basal plane; therefore such dislocations are obstacles for moving dislocations.

Twins are another type of obstacles. Twinning plays an important role in plastic deformation of *hcp* magnesium alloys. Our experiments were performed in compression. It was shown [22-24] that $\{10\bar{1}0\}$ compressive twinning, $\{10\bar{1}1\}$-$\{10\bar{1}2\}$ double twining and $\{10\bar{1}3\}$-$\{10\bar{1}2\}$ double twinning could also accommodate compressive strains along the c-axis at lower temperatures. The nearly constant level or slightly decreasing tendency of the internal stress estimated at a temperature of 200 °C indicates a decrease in the dislocation density as a consequence of recovery process/-es. With rising temperature, the intensity of dynamic recovery is increasing – this can be related to dislocation climb and also to the activity of additional non-basal slip systems. It should be mentioned that <*c*> dislocations are not able to glide (conservative movement) in the basal plane, however they may climb at elevated temperatures and release the primary glide. Another dislocation reaction may yield a sessile **<*c*+*a*>** dislocation:

$$\frac{1}{3}\left\langle 2\bar{1}\bar{1}3\right\rangle + \frac{1}{3}\left\langle \bar{1}2\bar{1}0\right\rangle \rightarrow \frac{1}{3}\left\langle 11\bar{2}3\right\rangle. \tag{9}$$

A combination of two glissile**<*c*+*a*>** dislocations gives rise to a sessile dislocation of <*a*> type that lays along the intersection of the second order pyramidal planes according to the following reaction:

$$\frac{1}{3}\left\langle 2\bar{1}\bar{1}3\right\rangle + \frac{1}{3}\left\langle \bar{1}2\bar{1}\bar{3}\right\rangle \rightarrow \frac{1}{3}\left\langle 11\bar{2}0\right\rangle. \tag{10}$$

It can be seen that different dislocation reactions may produce both sessile and glissile dislocations. Production of sessile dislocations increases the density of the forest dislocations that are obstacles for moving dislocations. Therefore, an increase in the flow stress with straining (i.e. hardening) follows, which is observed in the experiment.

Dislocations may be stored in front of impenetrable, thermally stable, precipitates and therefore dislocation pile-ups can be formed. These pile-ups are very effective stress concentrators. Local stress produced by the dislocation pile-ups may support cross slip of screw dislocations and so contribute to softening of the alloy. A higher density of precipitates in AJ91 and AX91 alloys compared with AJ51 and AJ41 alloys is the main reason for higher values of the CYS/TYS observed at lower temperatures. On the other hand, the precipitates (significant stress concentrators) may make easier climb of dislocations at elevated temperatures. Higher mobility of dislocations in prismatic and pyramidal slip planes at elevated temperatures increases the probability of dislocation reactions between **<*c*+*a*>** dislocations leading to dynamic recovery in a *hcp* structure.

6. Influence of solute atoms on activation volume

While the internal stress is strongly influenced with the content of solute atoms, the effective stress was– up to 100 °C–not affected by solute atoms (in the case of AJxy and AXxy alloys). The observed increase of the effective stress at higher temperatures is not surprising; the thermally activated process at higher temperatures is complex. Solute atoms (or their small clusters) are considered as typical local obstacles for moving dislocations. In high-temperature regime, diffusion-controlled glide should be taken into account.

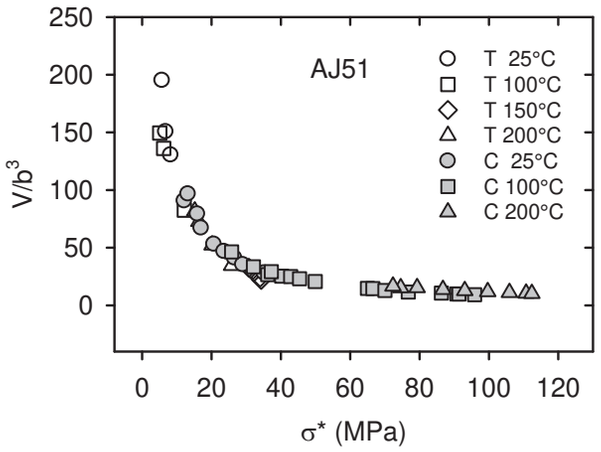

Figure 42. The plot of the activation volume in b^3 against the effective stress σ* for AJ51 alloy deformed in tension and compression at various temperatures.

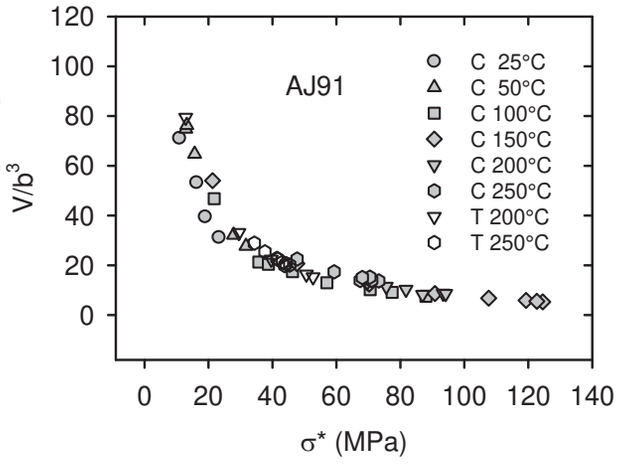

Figure 43. The plot of the activation volume in b^3 against the effective stress σ* for AJ91 alloy deformed in tension and compression at various temperatures.

http://dx.doi.org/10.5772/58949

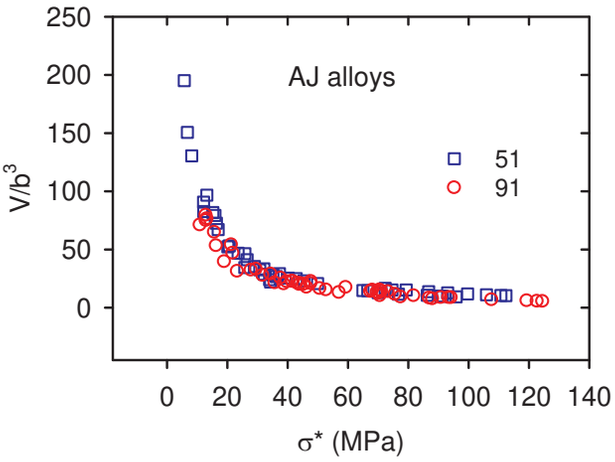

Figure 44. The plot of the activation volume in b^3 against the effective stress σ* for AJ51 and AJ91 alloys in tension and compression at all temperatures.

The values of the activation volume, V, were estimated in the stress relaxation experiments using equation (6). As usual, the values of the activation volume divided by b^3 for samples of AJ51 and AJ91 alloys deformed in tension as well as compression are plotted against the effective stress σ* for all testing temperatures in Figs 42-43 for tension (empty characters) and compression (full characters) deformation. The same analysis was performed for AX41 and AX91 alloys as it can be seen in Figs. 45-47. Plotting values of V against the effective stress for both AJ alloys into one diagram (Fig. 44) and those for both AX alloys in Fig. 47 shows that the activation volumes decrease with the effective stress and all the values lie on one line –"master curve". Kocks et al. [25] suggested an empirical equation between Gibbs free energy ΔG and the effective stress σ* in the following form:

$$\Delta G = \Delta G_0 \left[1 - \left(\frac{\sigma^*}{\sigma_0^*} \right)^p \right]^q , \tag{11}$$

where ΔG_0 and σ_0^* are Gibbs energy and the effective stress at 0 K. For the effective stress it follows:

$$\sigma^* = \sigma_0^* \left[1 - \left(\frac{kT}{\Delta G_0} \ln \frac{\dot{\varepsilon}_0}{\dot{\varepsilon}} \right)^{1/q} \right]^{1/p} , \tag{12}$$

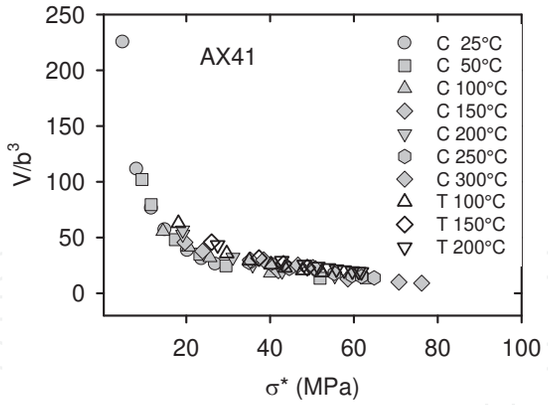

Figure 45. The plot of the activation volume in b^3 against the effective stress σ* estimated for AX41 alloy at various deformation temperatures in tension and compression.

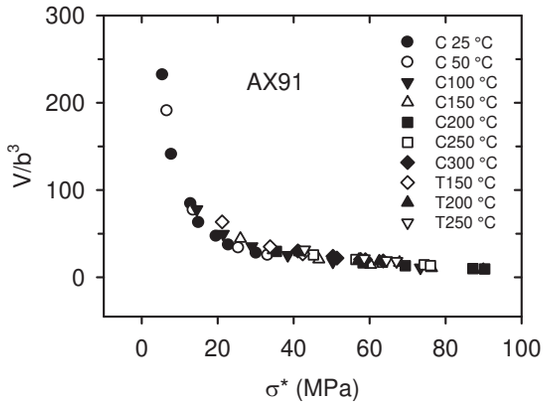

Figure 46. The plot of the activation volume in b^3 against the effective stress σ* estimated for AX91 alloy at various deformation temperatures in tension and compression.

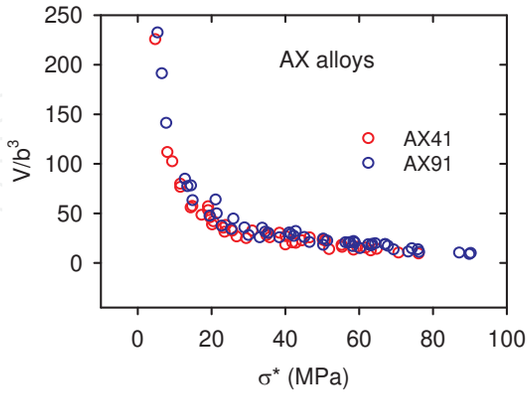

Figure 47. The plot of the activation volume in b^3 against the effective stress σ* estimated for AX41 and AX91 alloys at all temperatures in tension and compression.

where p and q are phenomenological parameters reflecting the shape of a resistance obstacle profile. The possible ranges of values p and q are limited by the conditions $0 < p \leq 1$ and $1 \leq$

http://dx.doi.org/10.5772/58949

q≤ 2. Ono [26], suggested that Equation (12) with p=1/2, q=3/2 describes a barrier shape profile that fits many predicted barrier shapes. Thermodynamics generally defines the activation volume as

$$V = -\left(\frac{d\Delta G}{d\sigma^*}\right)_T . \tag{13}$$

Equation (13) can be rewritten as

$$V = \frac{\Delta G_0 pq}{\sigma_0^*}\left[1-\left(\frac{\sigma^*}{\sigma_0^*}\right)^p\right]^{q-1}\left(\frac{\sigma^*}{\sigma_0^*}\right)^{p-1} . \tag{14}$$

The values of the activation volume should lie at the curve given by the equation (14). Results showing all values of the activation volumes being the same for alloys of AJ as well as AX series indicate that the thermal activation is not affected by various concentrations of solute atoms. It may be concluded that the thermally activated process(-es) is(are) determined with the dislocation motion and the solute atom role is less important. The values of the activation volume may help to identify thermally activated processes considering some of the common short−range barriers to dislocation motion [27]. The dislocation–dislocation interaction mechanism has an activation volume ranging from about 10^2–10^4 b^3, with the activation volume and enthalpy varying with strain. Couret and Caillard [28, 29] studied prismatic slip in magnesium in a wide temperature range using in situ experiments in TEM. They have reported that screw dislocations with the Burgers vector $1/3[11\bar{2}0]$ are able to glide on prismatic planes and their mobility is much lower than the mobility of edge dislocations. The deformation is controlled by thermally activated glide of those screw dislocation segments. A single controlling mechanism was identified as the Friedel−Escaig cross slip mechanism. This mechanism assumes dissociated dislocations on compact planes, like (0001), that joint together along a critical length L_r producing double kinks on non-compact planes. The activation volume is proportional to the critical length between two kinks. Amadieh et al. [30] found for the activation volume of the Friedel−Escaig mechanism a value of 70 b^3. Prismatic slip was also observed by Koike and Ohyama [31] in deformed AZ61 sheets. The activation of prismatic slip and subsequent annihilation of dislocation segments with opposite sign are probably the main reason for the observed internal stress decrease. The double cross slip may be a thermally activated process controlling the dislocation velocity. Beside this mechanism, the thermally activated glide of <***c+a***> dislocations should be taken into account. Mathis et al. [32] investigated the evolution of non−basal dislocations as a function of temperature in magnesium by X−ray diffraction. They found a majority of <***a***> dislocations in the as−cast state. During plastic deformation in tension the <***a***>−type dislocations remain dominant, however, the dislocation density increased by about a factor of three up to about 100 °C. At higher temperatures the fraction of <**c**+***a***>−type dislocations increased at the cost of <***a***>−type dislocations and the

increase of the dislocation density is strongly reduced. The internal stress acting on dislocations is determined by the details of the internal structure at that moment and it is independent of the applied stress. The stress that changes when the applied stress is changed is only the effective stress. The internal stresses during plastic deformation of the alloys investigated here can be considered as the sum of stresses resulting from various dislocation arrangements and obstacles existing in the deformed material [33, 34]. At higher temperatures the solute atoms may diffuse to stacking fault and may influence double cross slip from basal to non-basal planes.

7. Dynamic strain ageing (DSA) in magnesium alloys

Plastic deformation of alloys exhibits many phenomena associated with solute strengthening. When solute atoms can move (they may diffuse) during plastic deformation the microstructure of the deformed alloy is unstable. This microstructure instability is due to solute atoms diffusion towards to moving dislocations– the dynamic strain ageing (DSA) effect. The segregation of solute atoms at dislocations results in many phenomena:

- positive or non-monotonous dependence of the flow stress on temperature,
- negative strain rate sensitivity in a certain temperature range,
- post relaxation effect,
- local maximum in the temperature dependence of the activation volume or stress sensitivity parameter,
- the Portevin-Le Châtelier effect.

Magnesium alloys exhibit dynamic strain ageing effects at relatively low temperatures. Portevin-Le Châtelier effect (PLC) was observed during plastic deformation of some Mg alloys [35-39]. The unstable microstructure of an alloy can influence the deformation behaviour of the alloy. It should be mentioned that room temperature is high enough to help invoking strain ageing processes in magnesium alloys.

7.1. Portevin-Le Châtelier effect

The Portevin-Le Châtelier (PLC) effect is a consequence of a complicated nature of the dislocation dynamics in metals, which depends on many structural parameters as the type of structure, grain size, texture, concentration and distribution of solute atoms. Plastic deformation occurs inhomogeneously on the microscopic scale due to thermally activated dislocation motion through a field of obstacles. Deformation inhomogeneities in time and space, observed experimentally, are caused by collective dislocation motion. These phenomena of unstable plastic deformation are associated with the sharp localised deformation bands. Three types of PLC bands have been found. The continuously propagating type A, intermittently propagating type B with regular stress drops and stochastically nucleating type C. Figure 48 shows a representative microstructure of the undeformed Mg+0.7wt.%Nd sample after T6 temper

http://dx.doi.org/10.5772/58949

(homogenisation at 525 °C for 5h, then quenching into water 65 °C warm with subsequent precipitation treating for 8 h at 204 °C).

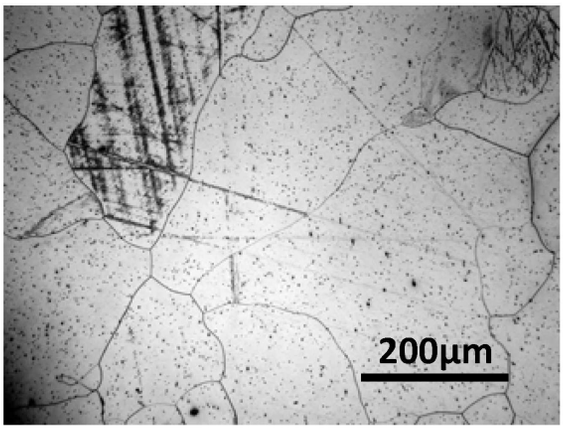

Figure 48. Microstructure of Mg-Nd alloy after T6 temper.

The true stress-true strain curves obtained at various temperatures are presented in Fig. 49 for tension and in Fig. 50 for compression tests. It can be seen a discontinuous character of curves obtained at elevated temperatures. Serrated yielding was observed at temperatures from 200 °C to 300 °C in tension and from 200 °C to 250 °C in compression. In compression tests the deformation at 300 °C was already smooth. While the shape of the serrations obtained in tension has character A, serrations found in compression have another shape, which is more of type B. PLC effect was also observed in an AZ91 (Mg-9Al-1Zn) alloy after thermal treatment T4 (homogenisation at 413 °C for 18 h, then quenching into water of ambient temperature). Tensile and compression tests were performed over a wide temperature range from 14 to 100 °C at an initial strain rate ranged in the 10^{-4} s^{-1}. The temperature dependence of the yield stress of Mg+0.7Nd exhibits a local maximum – a stress-hump (Fig. 51).

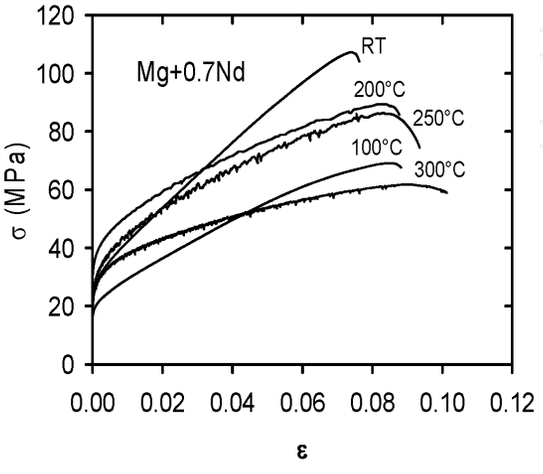

Figure 49. True stress-true strain curves of Mg+0.7Nd alloy deformed in tension.

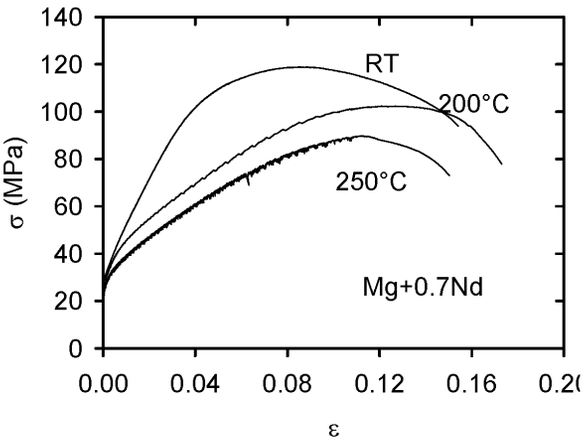

Figure 50. True stress–true strain curves of Mg+0.7 alloy deformed in compression at various temperatures.

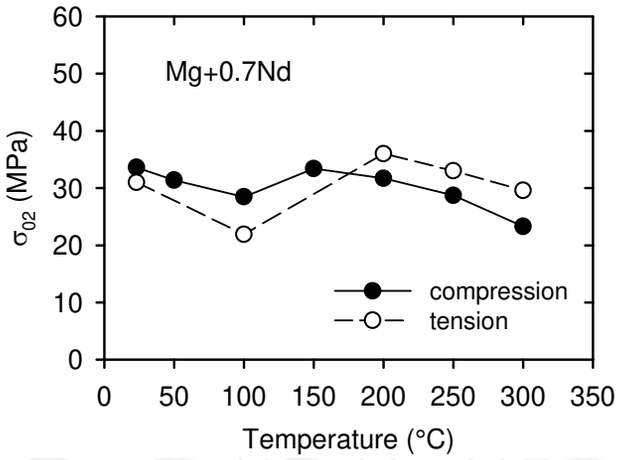

Figure 51. Temperature dependence of the yield stress of Mg+0.7Nd alloy deformed in tension and compression.

The stress-strain curve of AZ91 alloy obtained in tension at 21 °C is given in Fig. 52 together with the strain dependence of the strain hardening rate$\theta=d\sigma/d\varepsilon$. Serrations on stress-strain curves were observed at temperatures from room temperature up to 100 °C, the stress-strain curve obtained at temperature 150 °C exhibited no serrations; it was smooth. Similar experiments were performed in compression at an approximately same strain rate at temperatures from 15 to 100 °C. Character of serrations in compression is different in comparison with the tension tests as it is obvious from Fig.53. The stepwise character of curves indicates sudden elongation of the sample during the compression test.

http://dx.doi.org/10.5772/58949

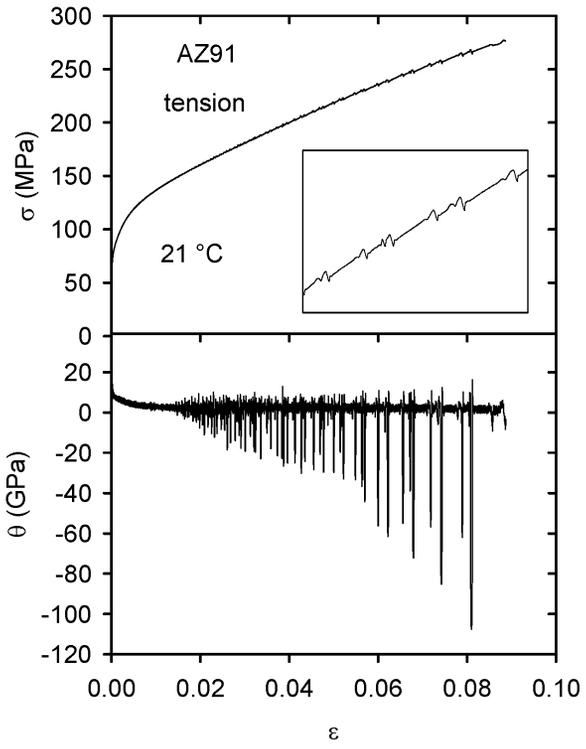

Figure 52. Stress-strain curve in tension obtained at 21 °C together with the strain dependence of the strain hardening rate.

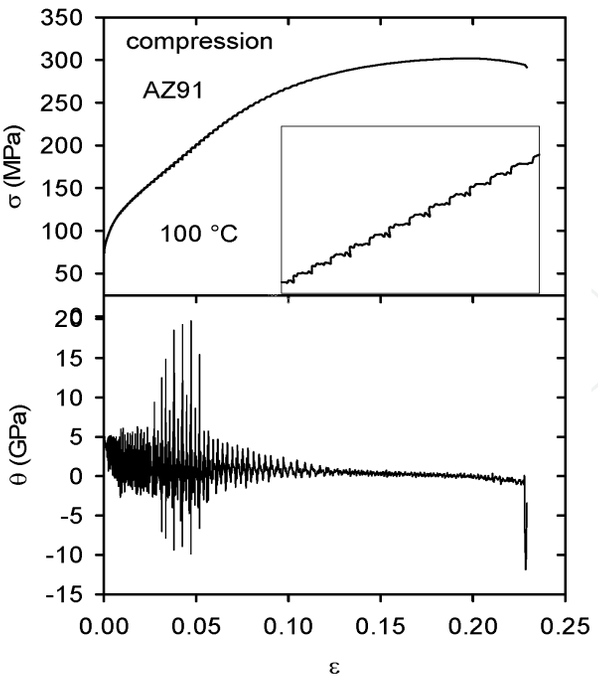

Figure 53. Stress strain curve and strain dependence of the strain hardening rate obtained in compression at 100 °C.

Lavrentev [40] have reported an important role of the dislocation forest in *hcp* structures with the main basal slip. Forest dislocations, which density was increased by prior movement of dislocation avalanche, are local obstacles for moving dislocations. Cores of dislocations waiting at forest dislocations during thermally activated motion in the slip plane may be occupied by solutes, which are movable due to pipe diffusion. These smaller dislocation groups of waiting dislocations are probably spread over a set of adjacent slip planes, rather than being strictly coplanar. They produce local stress concentrations, which may be a release pulse for break-away of dislocation pile ups. Precursor behaviour of the local strain associated with local stress relaxation prior to the strain avalanche may be characterised by the stress drop. This type of unstable flow is characteristic of the PLC flow, in which a drop in the load is possible if the strain rate during the formation of the slip bands exceeds the strain rate imposed by the tensile testing machine. A high level of the internal stress allow pass of these deformation bands through the whole sample. As each PLC band runs through the gauge length, the formation of new forest dislocations ensures that the process repeats itself. As the dislocation movement in the slip bands ceases or becomes too slow for the applied strain rate, for instance after a drop in the load or at the end of a PLC band, the applied stress must increase in order to resume deformation. Activation of new sources can only occurs by cutting through the forest dislocations created by secondary slip around slip bands no longer active. The forest dislocations increase the critical resolved shear stress for dislocation motion, but provide little strain hardening. If the activation of a source occurs under conditions of stable planar glide, dislocations can form a dynamic pile up able to move at increasing speed and decreasing levels of the applied stress because of the development of stress concentration ahead of the moving dislocations. This may spontaneously lead to an avalanche of dislocations that meets the general requirement for unstable tensile flow, since a drop in the load, as observed during the PLC effect, is possible only if the strain rate during the formation of the slip bands exceeds the strain rate imposed by the tensile testing machine. An additional factor is the following: as dislocations pile up in front of obstacles, the average dislocation velocity in the glide plane becomes very low so that moving solute atoms may diffuse towards the dislocations and pin them down.

7.2. Other manifestations of the dynamic strain ageing

The temperature dependence of the yield stress, σ_{02}, of Mg+0.7Nd alloy deformed in tension and compression (Fig. 51) shows that the course of the temperature dependence is non-monotonous. A local maximum in the temperature dependence of the yield stress obtained in compression and tension is observed in a temperature range of 150 – 250 °C.

Similar local minimum has been observed in the temperature dependence of the yield stress, σ_{02}, and the maximum compressive stress, σ_{max}, of ZE41 (Mg-4Zn-1RE) magnesium alloy as it can be seem in Fig. 54. While the local maximum in the temperature dependence is observed in alloys containing rare earths in the temperature interval 150-250 °C, alloys containing Al exhibit this local maximum between room temperature and 100 °C. This is demonstrated in Figs. 55 and 56 for AZ63 (Mg-6Al-3Zn) and AJ51 (Mg-5Al-0.6Sr), respectively. The strain rate dependence of the yield stress of Mg+0.7Nd alloy deformed in tension at 250 °C is presented

http://dx.doi.org/10.5772/58949

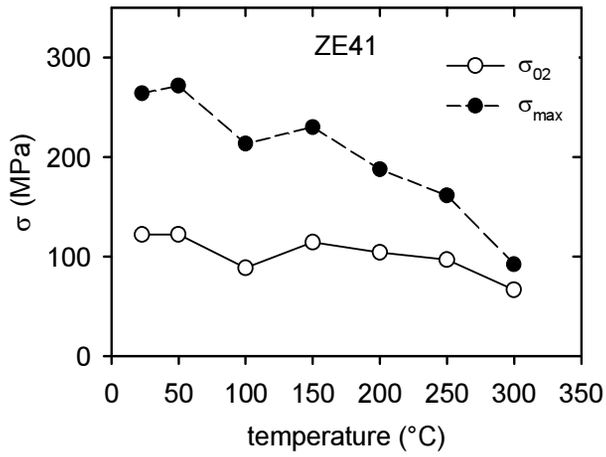

Figure 54. Temperature dependence of the yield and maximum stresses of ZE41 alloy

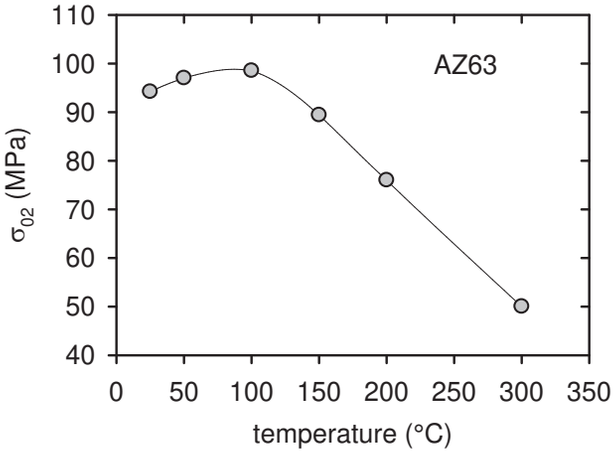

Figure 55. Temperature dependence of the yield stress of AZ63 alloy.

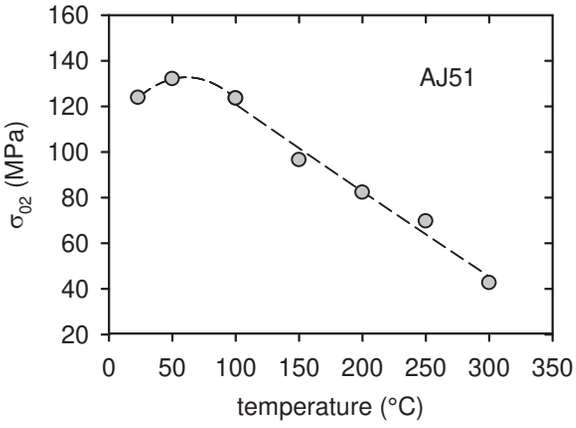

Figure 56. Temperature dependence of the yield stress of AJ51 alloy.

in Fig.57. Negative strain rate sensitivity was found for three strain rates from $5.5x10^{-5}$ to $5.5x10^{-4}$ s^{-1}. The strain rate dependence of the yield stress of ZE41 alloy deformed at three temperatures is given in Fig. 58. It can be seen that the strain rate dependences have an anomalous course. The yield stress usually increases with increasing strain rate. In this case, the yield stress increases only at lower strain rates. At strain rates higher than 10^{-4} s^{-1}, the yield stress decreases with increasing strain rate at 50 and 150 ºC. At 100 ºC the yield stress is practically independent of the strain rate. Again, the results indicate some dynamic strain ageing. It is also obvious that the values of the yield stress at 100 ºC are lower than those at 150 ºC at all imposed strain rates. Examples of short sequences of the stress strain curves of AZ91 alloy deformed at room temperature and two various strain rates are shown in Fig.59. It should be mentioned that the curves are not shifted; accordingly the negative strain rate sensitivity is obvious.

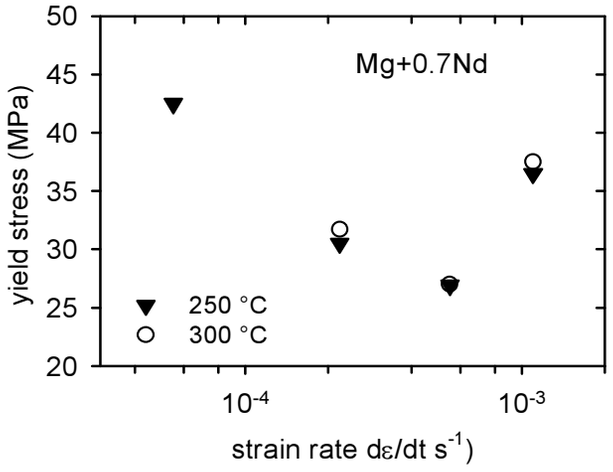

Figure 57. Strain rate dependence of the yield stress of Mg+0.7Nd alloy at two temperatures.

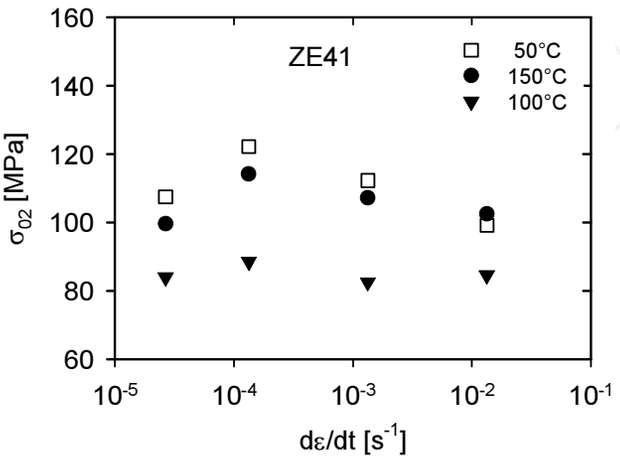

Figure 58. Strain rate dependence of the yield stress of ZE41 alloy deformed at three temperatures:

http://dx.doi.org/10.5772/58949

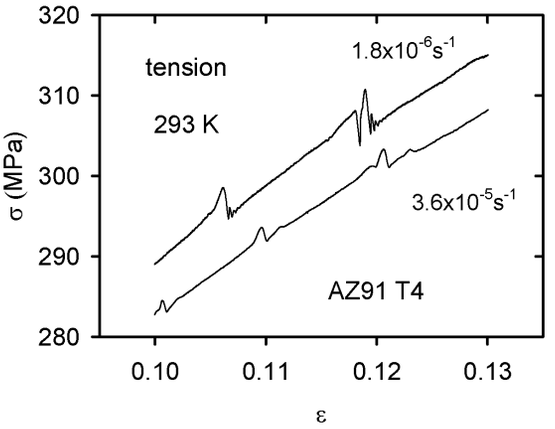

Figure 59. Sequences of the stress strain curves of AZ91 obtained for two strain rates. Negative strain rate sensitivity is obvious.

Very effective tool for studying of strain ageing phenomena are the stress relaxation tests. The SR curves are usually analysed assuming that the mobile dislocation density ϱ_m and internal stress σ_i are constant during the SR test. An unstable structure, changes in the mobile dislocation density and/or in the internal stress, may influence the course of the SR. In some SR tests, we observed a post relaxation effect. The flow stress at the beginning of deformation after stress relaxation σ_1 was higher (or lower) than the stress at the beginning of the stress relaxation $\sigma(0)$. The values of $\Delta\sigma=\sigma(0)-\sigma_1$ depend on strain, starting stress of the SR test and temperature. Examples of such dependences can be seen in Figs. 60-63 for magnesium alloys containing rare earth elements – Mg+0.7Nd alloy, ZE41 alloy, AE42 (Mg-4Al-2RE) and QE22 (Mg-2Ag-2RE). Similar dependences for alloys of the AZ series are presented in Figs. 64 and 65. It is obvious that the post relaxation effect is limited only on certain stress (strain) and temperature ranges. Local maxima are observed in these dependences. Such experimental results indicate that these phenomena are related to the dislocations and solute atoms mobility.

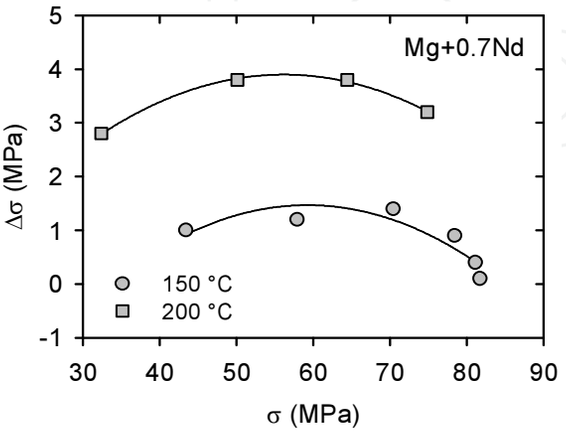

Figure 60. Dependence of the stress increment after the SR on the starting stress of SR estimated at two temperatures (Mg+0.7Nd).

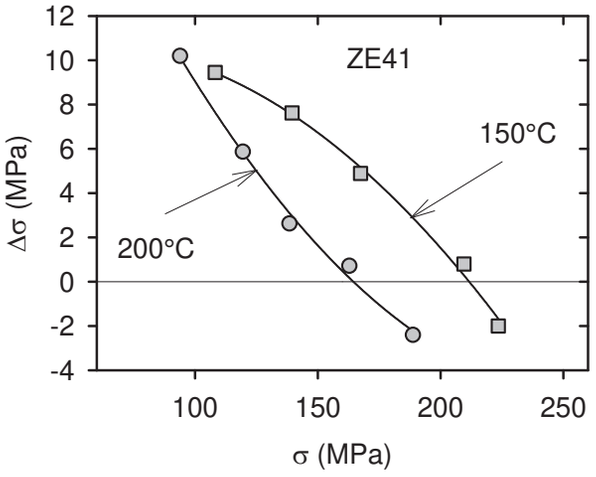

Figure 61. Dependence of the stress increment after SR on the starting stress of SR at two temperatures (ZE41 alloy).

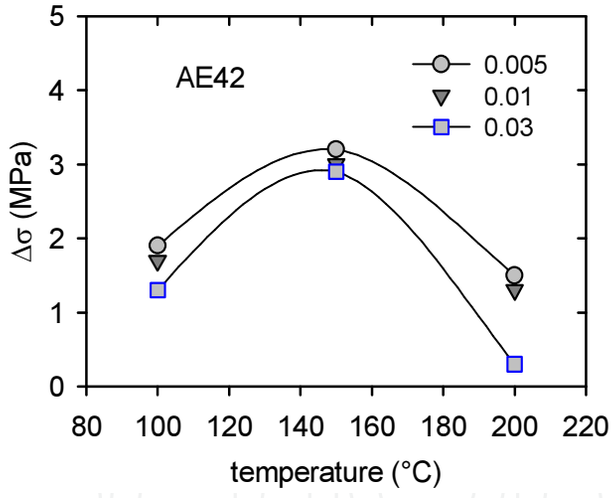

Figure 62. Temperature variation of the stress increment after SR at two starting strains of SR (AE42 alloy).

Solute atoms become mobile with increasing temperature. During a stress relaxation test, the dislocation velocity decreases, and at higher temperatures, the mobility of foreign atoms may be close to that of the dislocations. Thus, atmospheres of foreign atoms on dislocations may form. The dislocations are pinned by the solutes and hence, in order to restart their motion, they must be freed from the atmospheres after stress relaxation. Macroscopically, this results in a yield point due to dynamic strain ageing. The stress at the beginning deformation after the SR is higher than the stress at the beginning of the stress relaxation, which is observed experimentally.

http://dx.doi.org/10.5772/58949

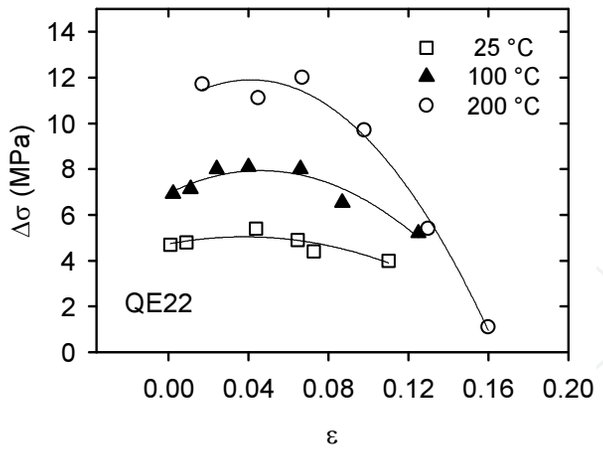

Figure 63. Strain dependence of the stress increment after SR at three temperatures (QE22 alloy).

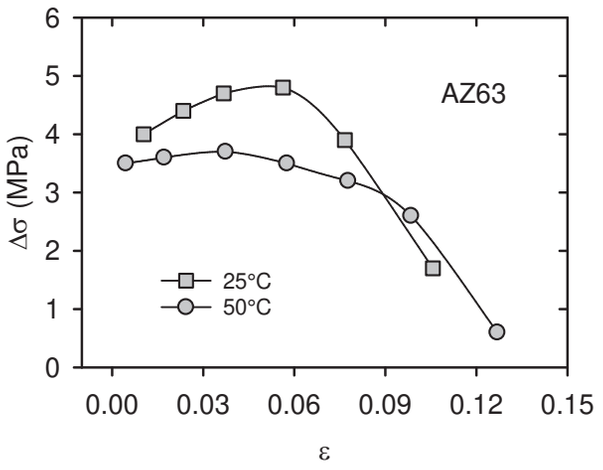

Figure 64. Strain dependence of the stress increment after SR at two temperatures (AZ63 alloy).

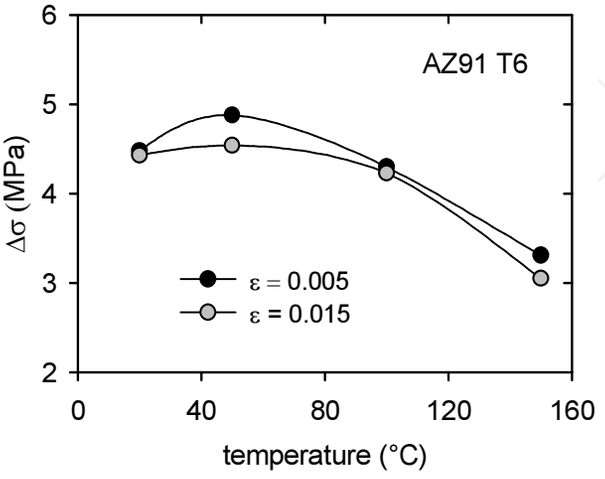

Figure 65. Temperature dependence of the stress increment after SR at two SR starting strains (AZ91 alloy).

The flow stress, necessary for the dislocation movement, may be expressed as a sum of two components

$$\sigma = \sigma_d + \sigma_f, \tag{15}$$

where σ_d is the dislocation component due to strong obstacles (e.g. forest dislocations, precipitates, grain boundaries) and σ_f is the friction stress due to the interaction between the solute atoms and moving dislocations. Mulford and Kocks [41] consider that the dislocation component of the flow stress rather than the friction stress is affected by dynamic strain ageing. Balík and Lukáč [42] take into account the influence of solute atoms on the both flow stress components in the dynamic strain ageing regime.

The local solute concentration increment, Δc, on the dislocations can be expressed as [43-45]

$$\Delta c = c - c_0 = \Delta c_M \left[1 - \exp\left(-t_a / t_0\right)^r \right]. \tag{16}$$

Here c is the local solute concentration in the dislocation core, c_0 is the nominal solute concentration in the matrix and Δc_M is the maximum concentration increment. The exponent r is equal 2/3 or 1/3 for bulk or pipe diffusion, respectively. The relaxation time t_0 depends on the binding energy between a dislocation and a solute atom, on solute concentration, and on the diffusion coefficient of solute atoms. t_0 is inversely proportional to the diffusion coefficient in the case of bulk diffusion, whereas for pipe diffusion $1/t_0 \sim D\rho_f^{3/2}$ [46], where ρ_f is the density of forest dislocations.

The mean ageing time t_a is identified with the mean waiting time t_w of mobile dislocations on the obstacles. t_w, is connected with the strain rate by the Orowan equation

$$\dot{\varepsilon} = b\rho_m \Lambda / t_w = b\Omega / t_w \tag{17}$$

where ρ_m is the mobile dislocation density, Λ is the mean free path of dislocations. If it is assumed that the forest dislocations are the rate controlling obstacles then $\Lambda = 1/\rho_f^{1/2}$. The elementary plastic strain per activation event $\Omega = b\rho_m \rho_f^{-1/2}$ is strain dependent; it may exhibit a local maximum at a certain strain [43, 44].

If we consider that both the dislocation stress component and the friction stress are influenced by solutes, then the flow stress may be decomposed into a non-aged part σ_{na} and a dynamic strain ageing part σ_a. The strain rate and temperature dependences of the stress increment due to dynamic strain ageing are simply related to the kinetic law $\Delta c(t_w)$ for the local concentration changes. Hence,

http://dx.doi.org/10.5772/58949

$$\sigma_a = \left(f_1 + f_2\right)\Delta c\left(t_w\right). \quad \text{(a)}$$
$$\text{or} \quad (18)$$
$$\sigma_a = \left(f_1 + f_2\right)\left[1 - \exp\left(-X\right)\right] \text{(b)}$$

The first term f_1 corresponds to the dislocation-dislocation interaction influenced by dynamic strain ageing, while the second term f_2 results from the solute atoms-dislocation interaction influenced by dynamic strain ageing. $X=(b\Omega/\ \dot{\varepsilon}\ t_0)$. Combining the relations (16) – (18), the negative strain rate dependence of the dynamic strain-ageing component follows. This causes the negative strain rate dependence of the yield stress, which is observed at certain temperatures and in a certain strain rate range. The negative slope in the strain rate dependence of the yield stress was also observed in Mg+0.7Nd alloy deformed at room temperature (Fig. 57). The observed decrease in the flow stress (negative values of $\Delta\sigma$) due to changes from a lower strain rate to a higher one is also the result of dynamic strain ageing.

Solute atoms locking dislocations cause the observed stress increase after stress relaxation, which depends on strain and on temperature. An increase in the flow stress is needed to move the dislocations after the stress relaxation. It is reasonable to assume that $\Delta\sigma$ is proportional to the number of impurities on the dislocation line. The density of dislocations increases with strain, while the concentration of solute atoms is constant. Thus, the stress increase, $\Delta\sigma$, after relaxation due to dynamic strain ageing should decreases with strain, which is observed. The value of Ω decreases with strain [44, 45] and hence, t_w also decreases. This leads to the observed decrease in $\Delta\sigma$. It should be mentioned that the post relaxation behaviour and the values of $\Delta\sigma$ depend also on the time of relaxation [47].

8. Nomenclature

Quantities (selected)	Alloys
σ, ε true stress, true strain;	LA40 Mg-4wt%Li
σ_i, internal (athermal) stress;	LA43 Mg-4wt%Li-3wt%Al
σ* effective (thermal) stress;	LA45 Mg-4wt%Li-5wt%Al
σ_f friction stress;	LA80 Mg-8wt%Li
σ_d dislocation stress;	LA83 Mg8wt%-Li-3wt%-Al
ΔG Gibbs free enthalpy;	LA85 Mg-8wt%Li-5wt%Al
V activation volume;	LA120 Mg-12wt%Li
$\dot{\varepsilon}$ plastic strain rate	LA123 Mg-12wt%Li-3wt%Al
b Burgers vector of dislocations	LA125 Mg-12wt%Li-5wt%Al
ϱ_m mobile dislocation density	AJ51 Mg-5wt%Al-0.6wt%Sr

Quantities (selected)	Alloys
ϱ_t total dislocation density	AJ91 Mg-9wt%Al-1wt%Sr
k Boltzmann constant	AJ62 Mg-6wt%Al-2wt%Sr
c atomic concentration of solute atoms	AX41 Mg-4wt%Al-1wt%Ca
CRSS critical resolved shear stress (τ_0)	AX62 Mg-6wt%Al-2wt%Ca
CYS compression yield stress (σ_{02})	AX91 Mg-9wt%Al-1wt%Ca
MCS maximum compression strength (σ_{max})	AZ63 Mg-6wt%Al-3wt%Zn
TYS tensile yield stress (σ_{02})	AZ91 Mg-9wt%Al-1wt.%Zn
MTS maximum tensile strength (σ_{max})	AE42 Mg-4wt%Al-2wt%RE
SR stress relaxation	ZE41 Mg-4wt%Zn-1wt%RE
SEM scanning electron micrograph	QE22 Mg-2wt%Ag-2wt%RE

Acknowledgements

Z.T. and P.L. are grateful for the financial support of the Czech Science Foundation (project P204/12/1360). P.P. is grateful for the financial support to the Slovak Grant Agency for Science (project VEGA No. 1/0797/12).

Author details

Zuzanka Trojanová[1], Peter Palček[2], Pavel Lukáč[1] and Zdeněk Drozd[1]

1 Charles University in Prague, Faculty of Mathematics and Physics, Czech Republic

2 University of Žilina, Faculty of Mechanical Engineering, Slovak Republic

References

[1] Haasen P. Mechanical Properties of Solid Solutions. In: Cahn RW, Haasen P, eds. Physical Metallurgy. 4th Edition, Amsterdam, Elsevier Science North Holland 1996, 2009-2073.

[2] Akhtar A, Teghtsoonian E. Solid Solution Hardening of Magnesium Single Crystals. Philosophical Magazine 1972; 25, 897-916.

[3] Stanford N, Barnett MR. Solute Strengthening of Prismatic Slip and {10-12} Twinning in Mg and Mg-Zn Binary Alloys. International Journal of Plasticity. 2013; 47, 165-181.

[4] Balík J, Lukáč P, Kužel R. Basal to Non-Basal Transition for In-Plane Deformation of AZ31 Magnesium Alloys. Acta Physica Polonica A 2012; 122(3), 435-438.

[5] Feltham P. Stress Relaxation in Magnesium at Low Temperatures. physica status solidi 1963; 3, 1340-1346.

[6] Levinson DW, McPherson DJ. Phase Relations in Mg-Li-Al Alloys. Transactions ASM 1956; 48, 689-705.

[7] Haferkamp H, Jaschik C, Juchmann P, Kaese V, Niemeyr M, Tai P. Entwicklung und Eigenschaften von Magnesium-Lithium-Legierungen. Materialwissenschaft und Werkstofftechnik 2001; 32, 25-30.

[8] Ando S, Tonda H. Non-Basal Slip in Magnesium-Lithium Alloy Single Crystals. Materials Transactions, Japan Institute of Metals 2000; 41, 1188-1191.

[9] Yoshinaga Y, Horiuchi R. On the Flow Stress of Solid Solution Mg-Li Alloy Single Crystals. Materials Transactions, Japan Institute of Metals 1963; 4, 134-141.

[10] Kamado S, Kojima Y. Deformability and Strengthening of Superlight Mg-Li Alloys. Metallurgical Science and Technolology 1998; 16, 45-54.

[11] Agnew SR, Yoo MH, Tomé N. Application of Texture Simulation to Understanding Mechanical Behavior of Mg and Solid Solution Alloys Containing Li or Y. Acta Materialia 2001; 49, 4277.

[12] Pawełek A, Piątkowski A, Kudela S, Jasieński Z. Acoustic Emission in Mg-Li-Al Alloys and Related Composites Based on Diphase α+β Matrix Subjected to Channel–Die Compression at Elevated Temperature 140 °C. Archives of Metallurgy and Materials 2006; 51, 245-252.

[13] Lukáč P, Balík J. Kinetics of Plastic Deformation. Key Engineering Material. 1994;97–98, 307–322.

[14] Pekguleryuz M. Creep Resistant Magnesium Alloys for Power-Train Applications. In: KU. Kainer (ed.), Magnesium Alloys and Their Applications. DGM, Willey-VCH 2003, 65-85.

[15] Trojanová Z, Lukáč P, Milička K, Száraz Z. Characterisation of Dynamic Strain Ageing in Two Magnesium Alloys. Materials Science and Engineering A 2004; 387–389, 80-83.

[16] Li JCM. Dislocation Dynamics in Deformation and Recovery. Canadian Journal of Physics 1967; 45, 493-509.

[17] Suzuki A, Saddock ND. Jones JW, Pollock TM. Structure and Transition of Eutectic $(Mg, Al)_2Ca$ Laves Phase in a Die-Cast Mg–Al–Ca Base Alloy. Scripta Materialia 2004; 51, 1005-1010.

[18] Ninomiya R, Ojiro T, Kubota K. Improved Heat Resistance of Mg-Al Alloys by the Ca Addition. Acta Metallurgica 1995; 43, 669-674.

[19] Gjestland H, Nussbaum G, Regazzoni G, Lohne O, BaugerØ. Stress-Relaxation and Creep Behaviour of Some Rapidly Solidified Magnesium Alloys. Materials Science and Engineering A 1991; 134, 1197-1200.

[20] Terada Y, Ishimatsu N, Sota R, Sato T, Ohori K. Creep Characteristics of Ca-Added Die-Cast AM50 Magnesium Alloys. Materials Science Forum 2003; 419-422, 459-464.

[21] Du W, Sun Y, Min X, Xue F, Zhu M, Wu D. Microstructure and Mechanical Properties of Mg–Al Based Alloy with Calcium and Rare Earth Additions. Materials Science and Engineering A 2003; 356, 1-7.

[22] Barnett MR. Twinning and the Ductility of Magnesium Alloys: Part II. "Contraction"Twins. Materials Science and Engineering A 2007; 464, 8-16.

[23] Koike J. Enhanced Deformation Mechanisms by Anisotropic Plasticity in Polycrystalline Magnesium Alloys at Room Temperature. Metallurgical and Materials Transaction A, 2005; 36A, 1689-1695.

[24] Jiang L. Jonas JJ, Mishra RK, Luo AA, Sachdev AK, Godet S. Twinning and Texture Development in Two Mg Alloys Subjected to Loading Along Three Different Strain Paths. Acta Materialia 2007; 55, 3899-3910.

[25] Kocks UF, Argon AS, Ashby MF. Thermodynamics and Kinetics of Slip. Progress in Materials Science 1975; 19, 1-288.

[26] Ono K, Temperature Dependence of Dispersed Barrier Hardening. Journal of Applied Physics 1968; 39, 1803-1806.

[27] Evans AG. Rawlings RD. The Thermally Activated Deformation of Crystalline Materials. physica status solidi 1969; 34, 9-31.

[28] Couret A, Caillard D. An in Situ Study of Prismatic Glide in Magnesium—I. The Rate Controlling Mechanism. Acta metallurgica 1985; 33, 1447-54.

[29] Couret A, Caillard D. An in Situ Study of Prismatic Glide in Magnesium—II. Microscopic Activation Parameters. Acta Metallurgica 1985; 33, 1455-62.

[30] Amadieh A, Mitchell J, Dorn JE. Lithium Alloying and Dislocation Mechanisms for Prismatic Slip in Magnesium Transactions AIME 1965; 233, 1130-37.

[31] Koike J, Ohyama R. Geometrical Criterion for the Activation of Prismatic Slip in AZ61 Mg Alloy Sheets Deformed at Room Temperature. Acta Materialia 2005; 53, 1963-72.

[32] Máthis K, Nyilas K, Axt A, Dragomir-Cernatescu I, Ungár T, Lukáč P. The Evolution of Non-Basal Dislocations as a Function of Deformation Temperature in Pure Magnesium Determined by X-ray Diffraction. Acta Materialia 2004; 52, 2889-2894.

[33] Milička K, Trojanová Z, Lukáč P. Internal Stresses During Creep of Magnesium Alloys at 523 K. Materials Science and Engineering A 2007; 462, 215-219.

[34] Trojanová Z, Lukáč P, Milička K, Száraz Z. Characterisation of Dynamic Strain Ageing in Two Magnesium Alloys. Materials Science and Engineering A 2004; 387-389, 80-83.

[35] Chatuverdi MC, Lloyd DJ. Onset of Serrated Yielding in Mg-10Ag Alloy. Philosophical Magazine 1974; 30, 1199-1207.

[36] Gärtnerová V, Trojanová Z, Jäger A, Palček P. Deformation Behaviour of Mg–0.7 wt. % Nd Alloy. Journal of Alloys Compounds 2004; 378, 180-183.

[37] Zhu SM, Nie JF. Serrated Flow and Tensile Properties of a Mg–Y–Nd Alloy. Scripta Materialia 2004; 50, 51-55.

[38] Corby C, Cáceres CH, Lukáč P. Serrated Flow in Magnesium Alloy AZ91. Materials Science and Engineering A. 2004; 387-389, 22-24.

[39] Trojanová Z, Cáceres CH, Lukáč P, Čížek L. Serrated flow in AZ91 Magnesium Alloy in Tension and Compression. Kovove Materialy-Metallic Materials 2008; 46, 249 – 256.

[40] Lavrentev FF. The Type of Dislocation Interaction as the Factor Determining Work Hardening. Materials Science and Engineering A 1980; 46, 191-208.

[41] Mulford RA, Kocks UF. New Observations on the Mechanisms of Dynamic Strain Aging and of Jerky Flow. Acta Metallurgica 1979; 27, 1125-1134.

[42] Balík J. Lukáč P. On the Kinetics of Dynamic Strain Ageing. Kovove Materialy-Metallic Materials 1998; 36, 3-9.

[43] Kubin LP, Estrin Y. Evolution of Dislocation Densities and the Critical Condition for the Portevin-Le Châtelier Effect. Acta Metallurgica et Materialia 1990; 38, 697-708.

[44] Balík J, Lukáč P. Portevin-Le Châtelier Instabilities in Al-3Mg Conditioned by Strain Rate and Strain. Acta Metallurgica et Materialia 1993; 41, 1447-1454.

[45] Louat N. On the Theory of the Portevin-Le Châtelier Effect. Scripta Metallurgica 1981; 15, 1167-1170.

[46] Friedel J. Dislocations. Pergamon, Oxford, 1964.

[47] Balík J. The Onset of Portevin– Le Châtelier Instabilities in Tensile Testing. Materials Science and Engineering A 2001; 316, 102-108.

IntechOpen